Eindhoven University of Technology

MASTER

Robust Measurement of Paper Fiber Surface Hygroexpansion using Global Digital Height Correlation

Verschuur, Nick A.M.

Award date:
2018

Link to publication

TU/e Technische Universiteit
Eindhoven
University of Technology

Robust Measurement of Paper Fiber Surface Hygroexpansion using Global Digital Height Correlation
Final report

Author
N.A.M. Verschuur
0915019

Supervisor
dr.ir. J.P.M. Hoefnagels
dr.ir. R.H.J. Peerlings

Date
28 March 2018

Where innovation starts

Preface

This thesis report is the final product of my graduation project, part of the master Mechanical Engineering at the Eindhoven University of Technology. The graduation project was done in the previous 8 months and during this period I got the chance to use my practical and theoretical knowledge to finish this project.
First, I would like to thank dr.ir. J.P.M. Hoefnagels and dr.ir. R.H.J. Peerlings for their coaching and advice during my project. Secondly, I want to thank Marc van Maris for his guidance and advice during the experiments. Finally, I would like to thank ir. S. Shafqat for his assistance on several topics of the project.

Nick Verschuur
's-Hertogenbosch, 28 March 2018

Technische Universiteit
Eindhoven
University of Technology

Table of contents

Title

Robust Measurement of Paper Fiber
Surface Hygroexpansion using Global
Digital Height Correlation

Where innovation starts

Abstract

During this project a methodology is developed and optimized to measure the hygroscopic displacement and strains of single fibers under changing relative humidity conditions. This methodology can be used to extract full-field measurements of displacements on a single fiber surface. Vertical Scanning Interferometry is used to acquire fiber surface topology images at different relative humidities. Global Digital Height Correlation (GDHC) is used to correlate the acquired topology images and to extract the displacement fields. Results show that the methodology is capable of extracting 3D displacements and strain fields of the fiber surface. The extracted strains lie in the strain range as described in literature. The strain fields show a certain gradient over the entire strain fields which concludes that the hygroexpansion of single fibers is not strictly a uniform process. Therefore, the methodology is a suitable tool for finding the fiber properties and hygroexpansion behaviour during changing relative humidity conditions.

1   Introduction

The importance of natural and printed fibers has been increasing since they became a main component of many engineering products. In general, fibers are sensitive for environmental factors such as relative humidity. The relative humidity influences the moisture uptake of a fiber which changes the dimensions of a fiber, also called hygroexpansion [1].
In the case of paper sheets, the hygroexpansion of individual fibers causes buckling and cockling of paper sheets which give problems during printing [2]. To find a solution for the buckling and cockling problem, a better understanding of the hygroexpansion of the individual fibers is required [3]. Literature shows different experiments have already been conducted to obtain fiber properties which are influenced by the relative humidity. During these experiments different techniques (X-ray, interferometry and Atomic force microscopy) have been proposed for characterizing the fiber properties, like hygroexpansivity [4]–[8]. However, there are no robust experimental methods which can directly extract full-field strain measurements of single fiber surfaces during changing relative humidity.
Therefore, the main goal of this research is to develop a robust technique to measure and determine the displacement and strain fields of different types of fibers due to hygroexpansion. To this end, Global Digital Height Correlation (GDHC) will be used to correlate topographies of single fibers and displacement and strain fields will be extracted from it.
A single fiber undergoes a combination of rigid body motion and deformations due to a change in relative humidity. The use of GDHC is convenient since it can distinguish the rigid body motion from the deformation. However, topographies of the fiber surface will be needed at different relative humidities.
This report starts with chapter 2 in which useful background information is discussed about paper and fibers, in literature described hygromechanics of paper & fibers and their methods for measuring these hygromechanics. The working principle of Global Digital Height Correlation is discussed as well. Chapter 3 contains the final developed experimental methodology. This experimental methodology has been optimized during the project in different stages. A detailed description of these optimizations can be found in the appendices. Results obtained according to the methodology are discussed in Chapter 4. Finally, in Chapter 5, the main conclusions are drawn about the methodology and the results of the experiments are presented. Additionally, this chapter includes recommendations for future work.

2 Background

2.1 Structure of paper & fibers

Paper mainly consists out of wood fibers. Figure 2-1 shows an image of fibers in a cracked paper sheet made with a Scanning Electron Microscope. The manufacturing process of paper sheets starts with the pulping of wood chips. During the pulping these wood chips are ground and mixed with water into a pulp. The pulp is then put through a pounding and squeezing process called beating. At this point various additives can be added which influences the opacity and other properties of the final product. The pulp is then sprayed onto a wire where much of the water is extracted. Subsequently, the web is squeezed through a series of steam heated cylinders. As a result, water is drained off from the pulp and the pulp is pressed together into paper. Finally, the dried paper is wound on reels and is smoothened and compacted further on metal rollers. The paper may be further finished by receiving a coating. This coating consists of chemicals or pigments which are added to the surface of the paper sheet. The manufacturing process and the individual fibers determine the mechanical, optical and hygroscopic properties of the paper sheet.

The wood fibers used in paper sheets have a length of 1-3 mm and a width of 20-50 μm [9]. The wood fibers consist of 4 different layers as shown in Figure 2-2. The different layers consist of mircofibrils and are designated as: the primary cell wall (P), the outer layer (S1), the middle layer (S2) and the inner layer (S3) of the secondary cell wall. Each layer is composed of several polymers: cellulose fibrils, hemicellulose and lignin. The secondary fiber wall (S2 layer) forms the main part of the single fiber. The S2 layer has a helical structure where the cellulose mircofibrils are wound around the axis of the fiber at an angle. This angle is called the microfibril angle (MFA). Since the middle layer forms the main part of a single fiber it has a large influence on the mechanical and physical properties of the fiber [10].
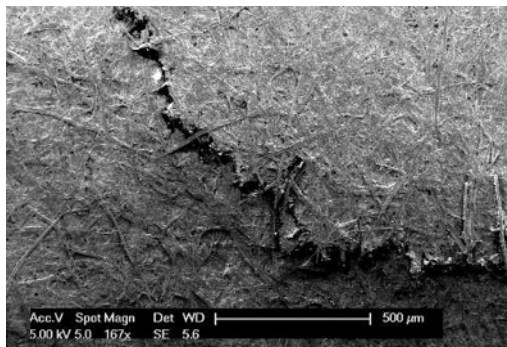

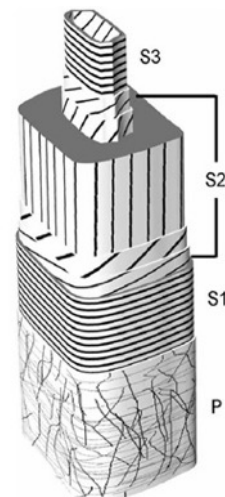*Figure 2-1: SEM image of fibers in a cracked paper sheet.*

Figure 2-2: Single fiber layers, with the primary unordered layer at the surface, the more ordered secondary layers S1, S2 and S3 [17]*.*

2.2   Hygroexpansion of fibers

Paper sheets can undergo hygroexpansion due to the moisture uptake from the environment. The structure of the fiber network changes due to displacements and reorientations of fibers. If the moistening of a paper sheet is inhomogeneous different reactions can occur, such as curling, buckling or the appearance of waviness. This behaviour can be noticed on a paper sheet that undergoes local wetting during water-based inkjet printing. These dimensional changes have a negative influence on the quality of the printing process. Because inkjet printing might be a dominant technology for printing in the future, printing companies (like Océ) want to improve this technology. To improve this technique a better understanding of the mechanics of hygroscopic dimensional changes of paper sheets is needed. Therefore, it is necessary to look at the hygromechanics of individual paper fibers.

A single fiber undergoes curling and twisting when it gets in contact with moisture, see Figure 2-3 and Figure 2-4. These deformations happen due to the hygroexpansion of the fiber. Commonly known in literature, over the range of 0-100% humidity, a fiber can expand about 1% in the longitudinal direction and about 20-30% in the transverse direction [1].

Figure 2-3: Single paper fiber before wetting.

Figure 2-4: Single paper fiber 10 minutes after wetting.

Literature shows different experiments have already been reported to obtain fiber shrinkage in longitudinal and transverse direction which are influenced by the relative humidity. The results of these experiments are discussed below and the used experimental methodologies are discussed in Section 2.3. Meylan [4] conducted experiments to determine the longitudinal shrinkage of Pinus radiate samples. Figure 2-5 shows three typical curves of longitudinal shrinkage against moisture content for one complete cycle for three samples. These samples had different mean microfibril angles but similar density (0.33 g/cm^3), wall thickness (2.04 μm) and cell dimensions (35.2 μm). From this Meylan concluded that the relation between the microfibril angle and the longitudinal shrinkage is non-linear and there is a hysteresis effect. As can be seen, the microfibril angle has a large influence on the final longitudinal shrinkage of a fiber. When the microfibril angle is increased from 11.5° to 39° the longitudinal shrinkage increases with 1.55%.
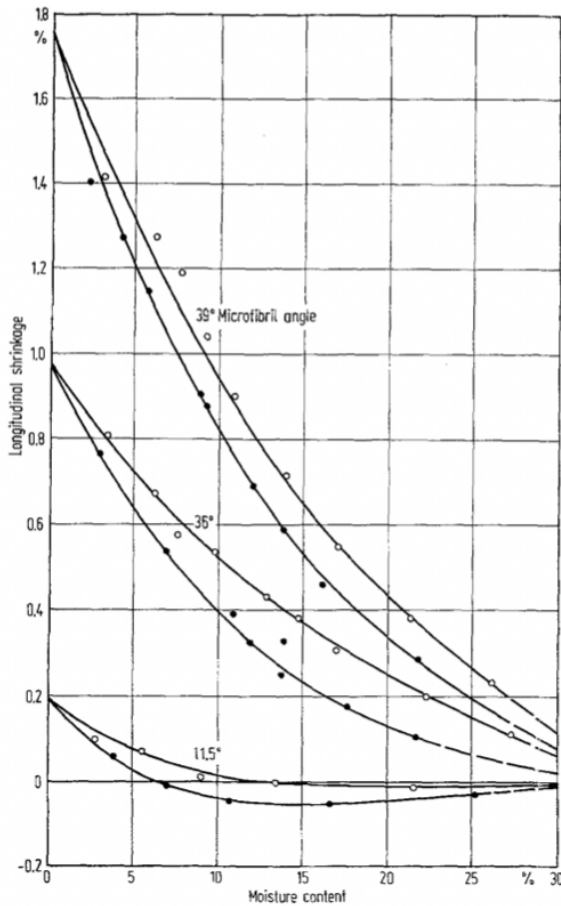
Figure 2-5: Longitudinal shrinkage as a function of moisture content for one complete moisture content cycle, for samples of different microfibril angles [4].

Yamamoto et al. [5] conducted research on the swelling and shrinkage of wood specimens. Thin and small rectangular flat-sawn wood fibers are used as specimens. Also in this paper the influence of the microfibril angle on the shrinkage is reported, see Figure 2-6. When the microfibril angle is below 30 degrees, the transverse direction reaches a shrinkage of 7~9%.
The longitudinal shrinkage is less than 1%. However, when the microfibril angle is above 30 degrees the longitudinal shrinkage becomes larger and the transverse shrinkage decreases. The maximum transverse strain from this experiment is considerably lower than the 20-30% strain which is mentioned earlier by Niskanen [1]. This is probably due to the samples, since Yamamoto et al. assumed that the shrinkage behaviour of the thin specimens are approximately equal to that of a single wood fiber which turns out to be unlikely.

Figure 2-6: Relationship between shrinkage and the microfibril angle of wood fibers [5].

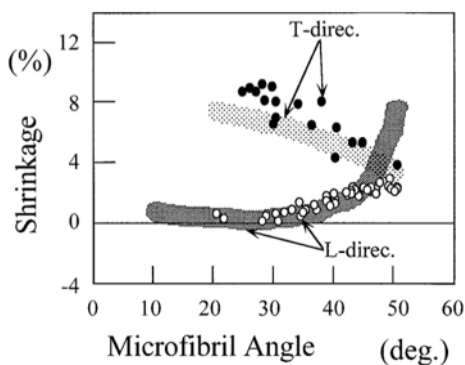Figure 2-7 represents the longitudinal shrinking of four different specimens, which microfibril angles in the S2 layers are 31, 38, 41 and 48 degrees. All the specimens started to shrink from a moisture content of 30%. The shrinkage curve tends to bend upwards when the microfibril angle is increased. For all the specimens the shrinking process between 5 and 20% is a linear process. However, the slope of the curves seems to decrease when the moisture content is lower than 5% or higher than 20%. Figure 2-8 represents the transverse shrinking for three different specimens, whose microfibril angles in the S2 layers are 27, 45 and 50 degrees. The transverse shrinking starts at a moisture content of 30%, similar to the longitudinal case. In contrast with the longitudinal case, the curve of the transverse shrinking tends to bend downwards when the microfibril angle is increasing. In conclusion, the microfibril angle has a large influence on the final shrinking strain in longitudinal and transverse direction.
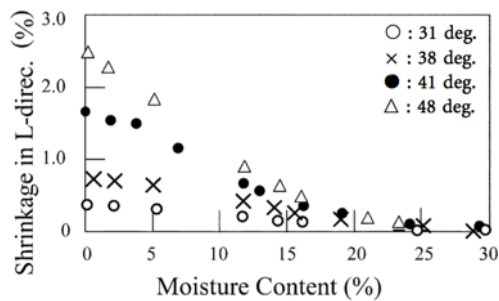

Figure 2-7: Longitudinal shrinking process from a 14-year-old sugi wood specimen with different microfibril angles [5].
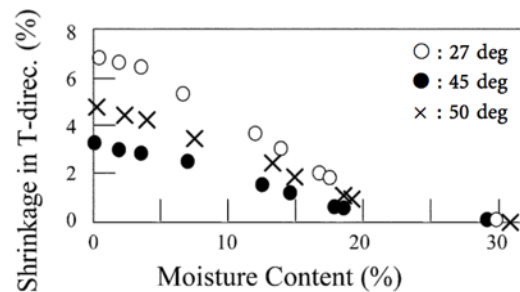
Figure 2-8: Transverse shrinking process from a 14-year-old sugi wood specimen with different microfibril angles [5].

Nanko and Wu [6] conducted experiments to determine the shrinkage of paper sheets, single fibers and fiber bonds. Worth nothing, the shrinkage of fibers is determined of fibers which are in a paper sheet. Figure 2-9 shows a schematic overview of a fiber from the fiber network which is measured by measuring the distances between the silver grains which are applied on the fibers, see Section 2.3 for the method. The longitudinal shrinkage of the fiber is determined by measuring the total shrinkage of the whole fiber (includes the fiber bonds). The shrinkage of the bonded segments is determined by measuring length B in Figure 2-9 and the shrinkage of the free segments is determined by measuring length F in Figure 2-9

Figure 2-9: Schematic overview of the silver grains on a fiber network [6].

Longitudinal shrinkage of the fibers in Japanese beech BKP were 30 to 80% larger than that of the sheet, see Figure 2-10. This longitudinal strain is larger than the mentioned strain of 1% by Niskanen [1] this is due to the bonds which

are present in the measured fiber. These bonds shrink more which causes a larger shrinkage rate of the whole actual fiber. Furthermore, the shrinkage rate of fibers as well as the sheet increased with an increased beating.
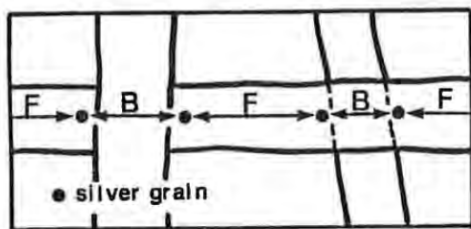
Also the effect of uniaxial restraining on the single fiber shrinkage was studied, see Figure 2-11. Restrained fibers are fibers which are aligned with an angle less than 45º to the restrained direction and those at an angle of larger than 45º were regarded as free fibers. The results show that the longitudinal shrinkage of a free fiber was more than 2 times larger than that of a restrained fiber. The longitudinal shrinkage of a free segment in the unrestrained direction is around 1%, which is the same according to Niskanen [1].
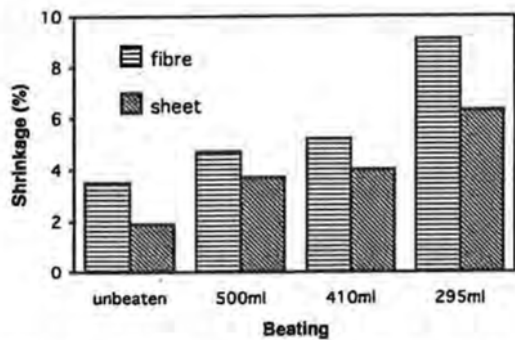
Figure 2-10: Shrinkage rate of a freely-dried sheet and its fibers [6].
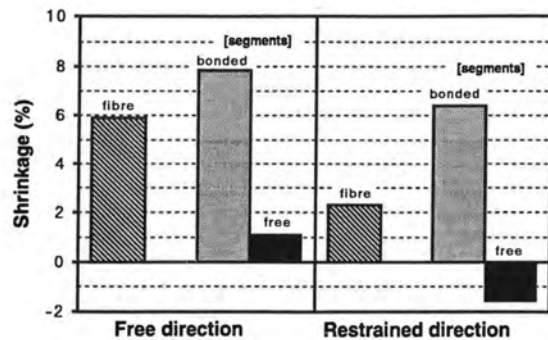
Figure 2-11: Average fiber shrinkage of fibers during uniaxially restrained drying [6].

Nanko and Wu concluded that the height information of a single fiber is needed to measure the actual shrinkage of a fiber. Figure 2-12 shows the surface change from a wet fiber and a dry fiber after restrained drying. With the projection method (see Section 2.3 for the explanation of this method) the fibers shrank only about 1% while the actual shrinkage of the fibers was 4%, see Figure 2-13.
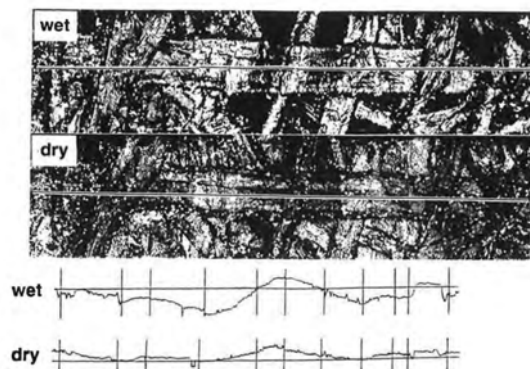
Figure 2-12: Change in the surface profile of a fiber due to restrained drying [6].
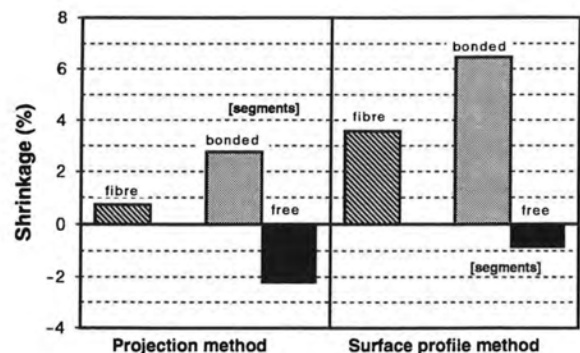
Figure 2-13: Difference in the average fiber shrinkage measured using the projection and surface profile method [6].

Besides the longitudinal shrinkage of fibers, the transverse shrinkage was also measured during the experiments. Both transverse and longitudinal shrinkage of the free fibers were larger than those of the restrained dried fibers, see Figure 2-14. These results show that the shrinkage is much higher in the transverse direction compared with the shrinkage in the longitudinal direction. The wall thickness of a fiber has a large influence on the transverse shrinkage but the influence on the shrinkage in the longitudinal direction is less.
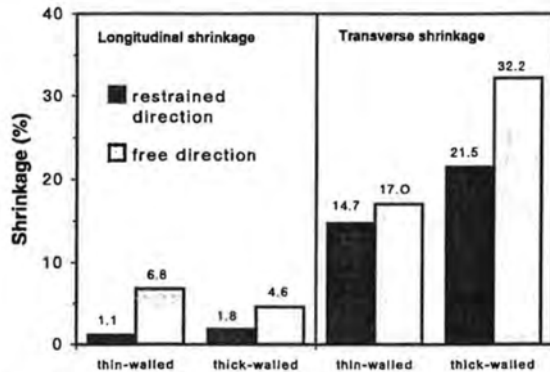
Figure 2-14: Transverse and longitudinal shrinkage of fibers during uniaxially restrained drying [6].

Lee et al. [7] conducted desorption and absorption experiments on single cellulose aggregate fibrils. Figure 2-15 represents AFM images taken from an area (10 μm x 10 μm) of a sample as a function of time during moisture desorption. After already 26 minutes of desorption the sample had undergone a significant deformation. As can be seen, a feature appears on the surface of the fibrils and it disappears again after 315 minutes of desorption. These features can be attributed to relaxation and plastic deformation of the fibrils. These dimensional changes occur during desorption but also during adsorption for most of the samples.
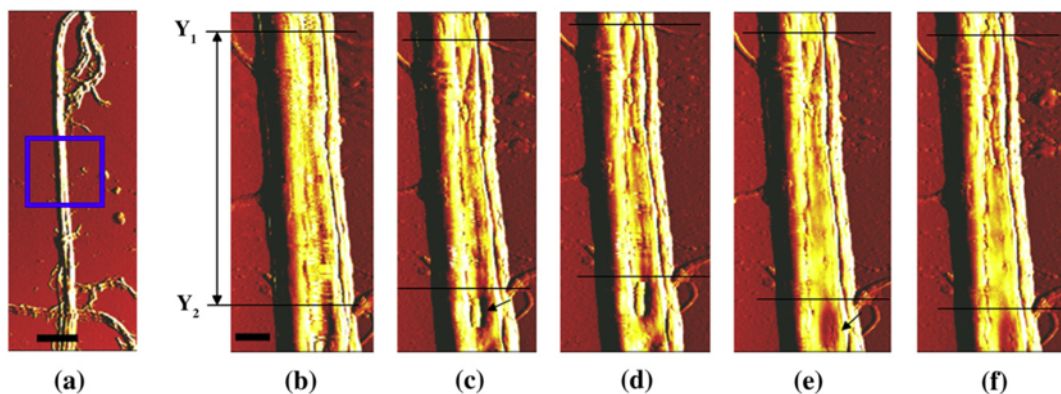
Figure 2-15: Tapping mode-AFM images of a cellulose aggregate fibril sample as a function of elapsed time under desorption stage. (a) Fiber area of 10 μm x 10 μm, (b) the sample subjected to the 80% RH, (c) 26 min elapsed after exposure to the ambient condition of 50% RH and 23 °C, (d) 70 min, (e) 315 min and (f) 1450 min elapsed [7].

Figure 2-16 shows the dimensional changes of three samples in desorption (left) and adsorption (right). The dimensional changes in the figure are given relative to the initial dimensions of the fibrils. These initial dimensions were determined at the ambient conditions before testing. In the desorption stage

the fibrils were exposed to 80% relative humidity for 24 hours before they were exposed to the ambient conditions of 50% relative humidity and 23 ºC. The length of the samples, exposed to ambient condition for 30 min, decreased by 10% in sample A and B, and 6% in sample C, compared to the initial sample size before exposure to high relative humidity. In time all the samples returned to their original length after 24 hours of exposure to the ambient conditions. Surprisingly, all dimensions decrease with an increased moisture content. Lee et al. assumed that these dimensional changes can be attributed to a rearrangement of the fibril structure. One explanation might be that the moisture content is weakening the bonds between the individual mircrofibrils. This increases the freedom of movement and allows the fibrils to rearrange into a structure of a lower energy state. Another explanation might be that defects (arrow marked features in Figure 2-15) occur at discrete locations along the length of the fibrils. Because of the moisture content uptake these defects swell. The cellulose chains must travel an arced path around these defects, which is longer. As a result, the cellulose chains will extend along the length of the fibril appear to contract and cause the fibril to shrink when water is taken up.

In the absorption stage the fibrils were exposed to 23% relative humidity for 24 hours before they were exposed to the ambient conditions of 50% relative humidity and 23 ºC. During adsorption the dimensional changes of sample A and B are showing some systematic variations. Sample C increased in all the dimensions, which would be more expected with the increase of moisture content. Overall, Lee et al. concluded that the dimensions of the cellulose aggregate fibrils during desorption and adsorption are responsive towards surrounding environments and the change in moisture content was more rapid than the relaxation of the single fibrils. The obtained results contradict the results of Nanko and Wu, Yamamoto et al. and Niskanen. For example, the resulted shrinkage in width direction is much higher than the transverse strains mentioned by Nanko and Wu, Yamamoto et al. and Niskanen. These large strain differences between the different studies can come due to large variations between fibers.
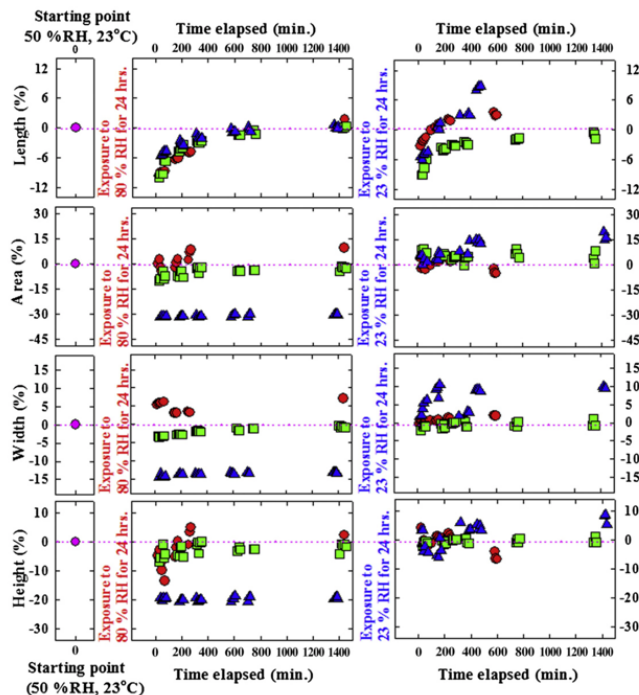

Figure 2-16: Dimensional changes of fibers (sample A (circles), sample B (squares), and sample C (triangles)) exposed to 80% RH for 24 hours, followed by returning to ambient condition of 50% RH and 23 ºC (left), and exposed to 23% RH for 24 hours, followed by returning to ambient condition of 50% RH and 23 ºC (right) [7].

Bastawrous [8] obtained displacement and strain fields for relative humidities between 15% and 90%, see Figure 2-17. The strain curves show the expected trend of increasing strain with an increased relative humidity and a decreasing strain with a decreased relative humidity. At 90% relative humidity, the longitudinal strain of the fiber is approximately 0.02, which is 2x smaller than the obtained transverse strain of 0.04. The dashed lines in Figure 2-17 represent the strain after it returns to 50% relative humidity after reaching a relative humidity of 15% or 90%. It can be seen that the fiber does not undergo irreversible changes after it has been conditioned at 15% relative humidity before it returned to 50% relative humidity. However, there is an irreversible change when the fiber is conditioned at 50% relative humidity after it was conditioned at 90% relative humidity. The fiber does not return to its initial state as there is a residual longitudinal strain of around 0.006 and a residual transverse strain of around 0.002. Bastawrous stated that conclusions about the underlying physics should be taken with caution. It is worth nothing that this work is not published since the accuracy and robustness are insufficient and were not yet optimized. The strains do not lay in the same range as the strains mentioned by Niskanen [1]. This can come due to the methodology since there is a lack of accuracy and robustness. This work is therefore unpublished.
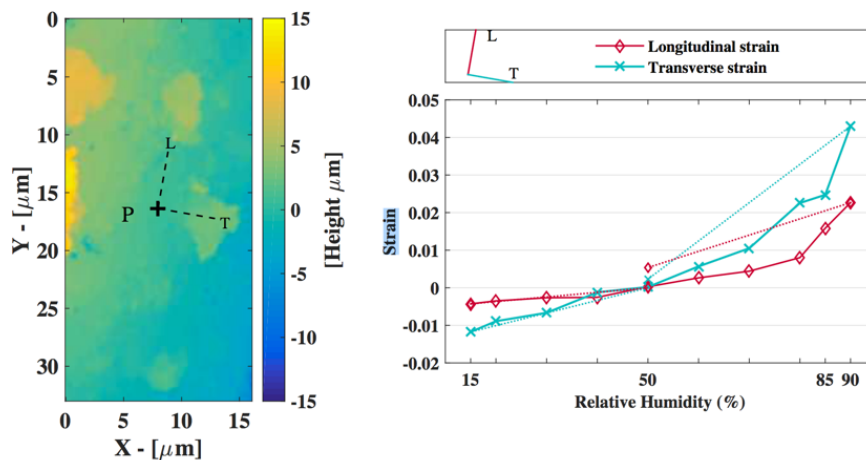
Figure 2-17: (a) Fiber surface at 50% RH, with point P at coordinates (8, 16.5) µm. (b) Longitudinal and transverse strains versus relative humidity values. The dashed lines indicate the strains after it returns to 50% relative humidity [8].

The table below represents a summary of the resulted strain ranges which are obtained in the above mentioned experiments for different types of fibers and fibrils during different ranges of relative humidities or moisture contents. It is remarkable that the strains in transverse and longitudinal direction fluctuate largely between the different results. For example, Niskanen works in the range of 0-100% relative humidity and talks about strains of 20-30% in the transverse direction and 1% in the longitudinal direction. However, Nanko and Wu are working in a relative humidity range of 60-100% and they talk about strains of 15-32% in transverse direction and 1-7% in the longitudinal

direction. So, they mentioned equal or even higher strains in a smaller range of relative humidity.

Another remarkable outcome is the largely negative transverse strain of -15% of Lee et al. This negative strain is very large compared to other mentioned strains which are in most cases positive. Worth nothing, all the authors used different types of samples which explains already the large fluctuations of the different strains.

Author(s)	Transverse strain range	Longitudinal strain range	Relative humidity range	Moisture content range
Niskanen [1]	20 to 30%	1%	0-100%	-
Meylan [4]	-	0 to 2%	-	0-30%
Yamamoto et al. [5]	4 to 8%	1 to 3%	-	0-30%
Nanko and Wu [6]	15 to 32%	1 to 7%	60-100%	-
Lee et al. [7]	-15 to 5%*	6 to 10%	50-80%	-
Lee et al. [7]	0 to 10%	3 to 6%	50-23%	-
Bastawrous [8]	0 to 5%	0 to 3%	15-90%	-

Table 2-1: Summarized results from literature.

* These results show large variations which is exceptional.

2.3   Methods for measuring hygroexpansion of fibers

In this section the methods which are used in the previous section are described. Meylan [4] used small blocks of wood (Pinus radiate) with a finished size of 2 mm x 2 mm in the transverse plane and 25 mm along the grain. The microfibril angles of these samples differed between 10º and 40º. These microfibril angles were measured by using X-ray diffraction. Three separate measurements were made in tangential and radial direction of each sample which were averaged to give a mean value.
The ambient conditioning was done in a conditioning apparatus, kept at 20ºC in a constant temperature room, in which the weight and dimensions of up to 10 samples at a time could be measured. The moisture content was determined by weighting the fiber during the experiments. This weighting was done by the use of a quartz helical spring. The relative humidity in the apparatus was controlled by circulating air over saturated salt solutions.
The samples were inserted with short pieces of drawn black glass of about 30 to 40 µm in diameter for radial and longitudinal measurements. The dimensions of the samples were measured by the use of an S.I.P.-Trioptic universal measuring machine.

Yamamoto et al. [5] used small rectangular flat-sawn specimens of a 14-year-old sugi. The specimens had a dimension of 50 x 10 x 2-5 mm in length, width and height direction and were used for longitudinal shrinkage. The specimens for the tangential shrinkage had a dimension of 10 x 20 x 2-5 mm in the respective directions.
The specimens were dried step by step in a desiccator by the use of saturated salt solutions. The weight and length of the specimens were measured at each equilibrium condition with an electric scale and a dial gauge. Every specimen was oven-dried for 24 hours at a temperature of 105°C. The oven-dried weight and length were used to determine the moisture content and the shrinkage of the specimen at every moisture content. The microfibril angle of every sample was determined by the use of X-ray diffraction.

Nanko and Wu [6] used two different types of pulp namely BKPs of Japanese red pine and Japanese beech that had never been dried. Wet webs of 60 g/m^2 were made using a laboratory sheet mold. The wet webs where then dried at 60% relative humidity at a temperature of 20°C under different restraining conditions:
- Free drying: The wet webs could dry without any restraint.
- Restrained drying: The wet webs were pressed to a plate and thus the web dried while sticking to the plate.
- Uniaxially restrained drying: Strips with a length of 100 mm and a width of 10 mm were cut from the wet web. The strips were then dried while being restrained along the long axis.

A silver powder was dispersed in water and pressed to a wet web by the use of a blotter. The silver particles were suitable as markers since they were small enough (1.4 µm diameter) and they were strongly reflected and were

hence easy to detect by the Scanning Laser Microscope (SLM). The powder was also highly dispersible in water and stayed on the fiber surface during drying. The silver grains on the fiber surface were used as location marks and by measuring the distance by hand between these silver grains the longitudinal shrinkage of a fiber could be determined in the XY plane (silver-grain method), see Figure 2-18.

To measure the actual fiber shrinkage, the deflection of the fiber in the Z-direction was taken into account as well. The surface measurement function of the SLM was used to measure the actual length of the fiber along its fiber surface (surface profile method). By combining the silver-grain method and the surface profile method the actual fiber shrinkage could be obtained.
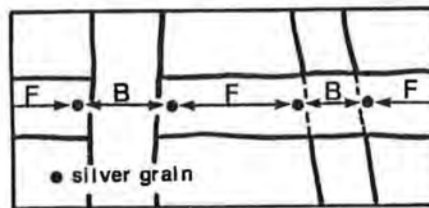

Figure 2-18: Measuring the fiber shrinkage on bonds and single fibers by the use of the silver-grain method [6]*.*

Lee et al. [7] used cellulose aggregate fibrils from a NIST bleached softwood kraft pulp. A glass slide with the cellulose aggregate was prepared by dropping 10 μl of diluted fibril suspension onto 20 different spots on a cleaned glass slide. The glass slide with the fibril sample was then dried in a controlled environment (50% relative humidity and 23 °C) for at least one week.

The relative humidity was controlled in a sealed container by the use of different saturated salt solutions. Different salts (ammonium chloride and potassium acetate) were used to obtain a relative humidity of 80% and 23%. Samples were allowed to equilibrate with the conditions inside the sealed container for 24 hours. After the conditioning the samples were quickly placed in the Atomic Force Microscope test chamber at 50% relative humidity and a temperature of 23°C. Images were made in times each image took approximately 10 minutes to complete. The elapsed time was recorded during all the scans. The images were made with a Q-scope^{TM} 250 using a NCS tip with a 230 μm long cantilever with a spring constant of approximately 3.5 N/m in intermittent contact mode. Two distinct defects (Y_1 and Y_2) were identified on the fiber surface. The difference in length between these defects was used to determine the changes in length during the experiments. The height, width and the cross-sectional area of the single fibers was determined after a processing algorithm of the gained AFM images [11].

Bastawrous [8] used a single pressed pulp fiber to measure the hygroexpansion due to a change in relative humidity. The fiber was glued at both ends on a glass slide, preventing it from twisting or moving outside the field of view.

The relative humidity was controlled in a humidity control box, shown in Figure 2-19a. The relative humidity was controlled by means of mixing a flow of dry

nitrogen and humidified air. A sample was placed inside this humidity control box and the box was placed under the optical confocal profiler (Sensofar PLμ 2300), shown in Figure 2-19a. The optical confocal profiler was used to obtain single fiber topographies at different relative humidities during the experiments, see Figure 2-19b. The fact that fibers are semi-transparent could lead to internal reflections of incident light rays from the profiler. These reflections could lead to unrealistic topographies of the fiber surface. To tackle this problem, the fiber surface was brushed with silver nano-particles to increase its opacity.

All the fiber surface topographies during an experiment were used to determine the displacements and strain fields over the whole fiber surface. The topographies were compared and correlated by the use of Global Digital Height Correlation.
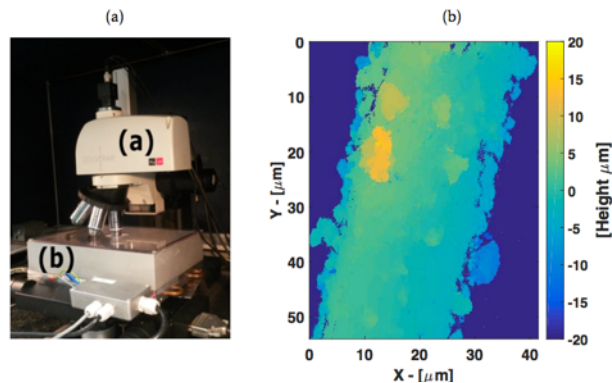
*Figure 2-19: (a) Experimental setup, where **(a)** is the optical confocal profiler (Sensofar Plμ 2300) and **(b)** is the humidity control box. (b) Obtained fiber topography by optical confocal profiling* [8].

All the described methodologies in this chapter proved their feasibility of measuring the hygroexpansion of fiber wood blocks, fibrils and single fibers. In this particular case we are interested in the methodology of Bastawrous. Because the methodology of Bastawrous seemed promising since this method can be used for generating full-field displacement and strain data of the fiber surface during relative humidity changes instead of generating an average displacement and strain for a single fiber. The working principle of the used Global Digital Height Correlation is further explained in Section 2.4.

2.4 Global Digital Height Correlation

In this section the working principle of Global Digital Height Correlation (GDHC) will be discussed. First we start with Global Digital Image Correlation (GDIC) since the GDHC works with the same formulations but is a sort of upgrade of the formulations.

Global Digital Image Correlation (GDIC) is a method to measure the displacement field between two images obtained at different stages of loading in an experiment. The first image is a picture of the reference state f, and the second image is a picture of the deformed state g.

Figure 2-20 represents a schematic tensile bar containing a speckle pattern. Assume that the bar is deformed by an unidirectional load F. The gray value in images $f(\vec{x}_0)$ and $g(\vec{x})$ can be correlated by GDIC to find the displacement field corresponding to all material points.

Consider one arbitrary material point P that has moved from position $\vec{x}_0$ in image f to position $\vec{x}$ in image g. The corresponding displacement vector $\vec{u}(\vec{x}_0)$ is found after the correlation. Positions $\vec{x}$ and $\vec{x}_0$ are related to each other by this displacement:

$$\vec{x} = \vec{x}_0 + \vec{u} \qquad\qquad (\,2.1\,)$$

Therefore, the brightness of image f and g are equal at the respective positions $\vec{x}_0$ and $\vec{x}$:

$$f(\vec{x}_0) = g(\vec{x}_0 + \vec{u}) \qquad\qquad (\,2.2\,)$$
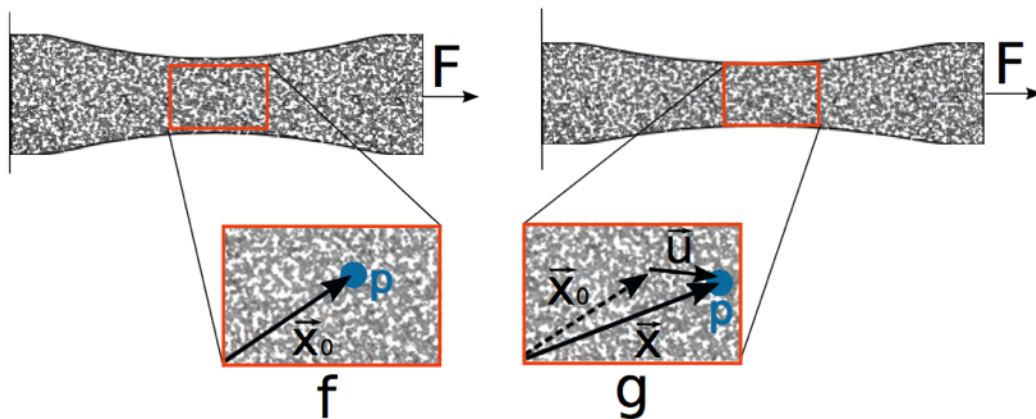
Figure 2-20: Illustration of DIC, where images f and g are correlated in order to find the full-field displacements u of the material points (e.g., point P) in the imaged tensile bar [12].

In order to find the displacement $\vec{u}$, the two images are subtracted from one another, which results in a so-called residual image:

$$\psi = f(\vec{x}_0) - g(\vec{x}_0 + \vec{u}) \qquad\qquad (\,2.3\,)$$

For a perfect displacement, the two corresponding positions of the material point have exactly the same grey scale brightness. The residual would in this case be identically equal to zero ($\psi = 0$). However, due to image noise and

errors during the correlation, the residual is never exactly zero. Finding the displacement is thus realized by minimizing the residual on the entire 2D-domain:

$$\Phi = \int_{\Omega_0} \psi^2 dx_0 dy_0 \qquad\qquad (\,2.4\,)$$

Ω_0 is the 2D-domain in which the material points reside. x_0 and y_0 correspond to the directions over which is integrated within this domain. The residual in 2D becomes:

$$\psi(\vec{x}_0) = f(\vec{x}_0) - \mathrm{g}(\vec{x}_0 + u(\vec{x}_0)\vec{e}_x + v(\vec{x}_0)\vec{e}_y) \qquad\qquad (\,2.5\,)$$

where u and v are the in-plane components of the displacement respectively in x and y direction, and ψ is the residual field.

From this point onwards we will talk about Global Digital Height Correlation (GDHC) instead of Global Digital Image Correlation (GDIC). In this case the images contain profilometric data. All the pixel values contain height information, which may evolve between two images. This height information is used instead of grey scale information. Thus the grey level conservation is rewritten as "topography" conservation:

$$\psi(\vec{x}_0) = f(\vec{x}_0) - \left(\mathrm{g}\left(\vec{x}_0 + u(\vec{x}_0)\vec{e}_x + v(\vec{x}_0)\vec{e}_y\right) - w(\vec{x})\right) \qquad\qquad (\,2.6\,)$$

where w denotes the out-of-plane displacement, and ψ is still the residual field. To determine the displacement field, Φ according to equation (2.4) is minimized, yielding the displacement field for which the residual field is smallest. However, minimization of Φ cannot be solved. The number of unknowns is namely exceeding the number of equations. To solve this problem, the number of degrees of freedom (DOFs) must be reduced. Therefore, the displacement field can be approximated by the use of a combination of shape functions $\vec{\varphi}(\vec{x}_0)$ and (a reduced number of) degrees of freedom λ. The shape functions can be thought of as functions that describe the form (shape) that a displacement field may take. The shape functions can restrict certain morphology of the displacement field, and thereby the number of corresponding DOFs is reduced. The approximation of the displacement field in terms of shape functions and DOFs is written as follows:

$$\vec{u}^*(\vec{x}_0, \underline{\lambda}) = \sum_{q=1}^{3m} \lambda_q \vec{\varphi}_q(\vec{x}_0) \qquad\qquad (\,2.7\,)$$

An approximation of the displacement field can be made for $u(\vec{x}_0)$, $v(\vec{x}_0)$ and $w(\vec{x})$:

$$u^*(\vec{x}_0, \underline{\lambda}) = \vec{u}^*(\vec{x}_0, \underline{\lambda}) \cdot \vec{e}_x \qquad\qquad (\,2.8\,)$$

$$v^*(\vec{x}_0, \underline{\lambda}) = \vec{u}^*(\vec{x}_0, \underline{\lambda}) \cdot \vec{e}_y \qquad\qquad (\,2.9\,)$$

$$w^*(\vec{x}_0, \underline{\lambda}) = \vec{u}^*(\vec{x}_0, \underline{\lambda}) \cdot \vec{e}_z \qquad\qquad (\,2.10\,)$$

which can be substituted into equation (2.6):

$$\psi(\vec{x}_0) = f(\vec{x}_0) - \left(g\left(\vec{x}_0 + u^*(\vec{x}_0, \underline{\lambda})\vec{e}_x + v^*(\vec{x}_0, \underline{\lambda})\vec{e}_y\right) - w^*(\vec{x}_0, \underline{\lambda}) \right) \qquad (\,2.11\,)$$

Minimizing of Φ given by equation (2.4) is done by finding the root of the derivative with respect to the degrees of freedom:

$$\forall_k \quad \Gamma_k = \frac{\partial \Phi}{\partial \lambda_k} = 0 \qquad\qquad (\,2.12\,)$$

To solve this non-linear problem, the iterative Newton-Raphson procedure is applied as described in more detail by Neggers et al. [13]:

$$\forall_k \quad \sum_{q=1}^{3m} \frac{\partial \Gamma_k^{it}}{\partial \lambda_q^{it}} \delta \lambda_q = -\Gamma_k^{it} \qquad\qquad \lambda_k^{it+1} = \lambda_k^{it} + \delta \lambda_q \qquad (\,2.13\,)$$

Hence, eventually the following linear system of equations must be solved successively:

$$\underline{\underline{M}}\,\delta\underline{\lambda} = \underline{b} \qquad\qquad (\,2.14\,)$$

Where $\delta\underline{\lambda}$ contains the iterative updates of the degrees of freedom and the correlation matrix $\underline{\underline{M}}$ and vector $\underline{b}$ are defined as:

$$b_k = -\Gamma_k^{it} = 2 \int_{\Omega_0} \left[\vec{G} \cdot \vec{\varphi}_k \psi \right] dA_0 \qquad\qquad (\,2.15\,)$$

$$M_{qk} = -\frac{\partial \Gamma_k^{it}}{\partial \lambda_q^{it}} = 2 \int_{\Omega_0} \left[\vec{G} \cdot \vec{\varphi}_k \vec{G} \cdot \vec{\varphi}_q \right] dA_0 \qquad\qquad (\,2.16\,)$$

$\vec{G}$ (in equation (2.15) and (2.16)) is a gradient operator of the image with respect to the spatial coordinates with an enrichment of an out-of-plane component. Different choices for the image gradient can be made, which have been explored in more detail by Neggers et al. [14]:

$$\vec{G}_1 = \frac{\partial f}{\partial x_0}\vec{e}_x + \frac{\partial f}{\partial y_0}\vec{e}_y - \vec{e}_z \qquad (\ 2.17\ )$$

$$\vec{G}_2 = \frac{\partial \tilde{g}}{\partial x_0}\vec{e}_x + \frac{\partial \tilde{g}}{\partial y_0}\vec{e}_y - \vec{e}_z \qquad (\ 2.18\ )$$

$$\vec{G}_3 = \tfrac{1}{2}(\vec{G}_1 + \vec{G}_2) \qquad (\ 2.19\ )$$

In general, $\vec{G}_1$ is convenient when close to the solution. Since it is the gradient of the reference image f, it can be calculated at the beginning of the correlation and does not need to be updated. It results in robust convergence. However, when further from the solution, $\vec{G}_2$ becomes more accurate. It is the gradient of the back deformed image. To combine the advantages of robustness and accuracy, a combination of $\vec{G}_1$ and $\vec{G}_2$ is often used, see equation (2.19). The above mentioned theory [12]–[14] had already been implemented in a matlab script which has been used during the project.

Besides the theory explanation also some terms need to be explained which are used later in this report:

Coarse graining: Coarse graining implies averaging 2 x 2 pixels into super-pixels. This operation can be repeated on the super pixeled images to create even coarser images, in a number of so-called coarse grain steps.
The correlation procedure starts on the coarsest image. The obtained values for the DOFs are then supplied as an initial guess to the next correlation step on a less coarse image, until arriving to the original, fine image. The coarse graining exponentially reduces the amount of pixels and therefore also the amount of DOFs. This results in a poorly defined outcome; but this is acceptable since the solution of a coarse grained step is only used as an initial guess for the next correlation with less coarse graining.

Convergence criterion: The convergence criterion is a criterion which determines if the nonlinear equation (2.12) have been solved to sufficient accuracy. The chosen criterion is such that the norm of the DOF increments, $\delta\lambda$, becomes sufficiently small, i.e.
$\|\underline{\delta\lambda}\| < 10^{-4}$.

Basis shape function: As described earlier, the shape functions can be thought of as functions that describe the form (shape) that a displacement field may take. These shape functions can have different basis, e.q. polynomial basis.

Order of the shape functions: The order of the shape functions determines the amount of degrees of freedom. The choice of the order of the shape functions determine the kinematic freedom of the solution space. Generally, adding too little kinematic freedom leads to an error since the shape function cannot fully

capture the actual kinematics in the fiber. In contrast, adding too much kinematic freedom increases the sensitivity to noise. A correlation can get stuck in a minimum and the iterative process will converge but the results are unreliable since it converges to a minimum. For that reason, it is important to use a basis function to fully capture the kinematics with a minimum order of that basis function.

Masking: The masking function masks specific pixels from the calculations. The specific pixels are chosen from the reference image f and are ignored in the backdeformed image $\tilde{g}$. The selected masked pixels can then be deleted from the correlation matrix $\underline{\underline{M}}$ and $\underline{b}$. Since the masked pixels are deleted from the correlation matrices they do not have any influence on the correlation.

3   Final optimized methodology

This chapter describes the final optimized methodology to measure the hygroscopic strain of individual fibers.

Previously PhD student Bastawrous worked on a method to extract full-field measurements of displacements on a single fiber surface during relative humidity changes, as mentioned in Section 2.3. The methodology of Bastawrous seemed promising since this method can be used for single fiber measurements during humidity changes. The main advantage of this method is the possibility of generating full-field displacement and strain data of the fiber surface during relative humidity changes instead of generating an average displacement and strain for a single fiber. However, the accuracy and robustness of the method and results were insufficient. The methodology was never further developed into a full robust method for extracting full-field measurements of displacements and strains on single fiber surfaces.

This formulates directly the goal for this project namely, optimizing the method proposed by Bastawrous, to obtain a more accurate and robust method. The optimizations can be found in:
- Sample preparation
    - Method for obtaining a single fiber from paper
    - A technique for fiber patterning
- Climate box setup
- Profilometry
    - Type of profilometer (Vertical Scanning Interferometry versus Optical Confocal profilometry)
    - Settings of the profilometer
    - Size of magnification
- GDHC settings
    - Method for creating reconstructed data
    - Order shape function
    - Masking

During the project different optimization steps were taken, which are all described in the Appendices A, B and C. Worth nothing is that some optimizations were a combination of different smaller optimizations.

Below we discuss the final optimized methodology. The results presented in Chapter 4 have been obtained using this methodology.

3.1   Sample preparation

Océ provided printing paper (Soperset premium 80 GR/M2 29-11-16) for the experiments, so that obtained results can be compared with other available data on this paper. This paper only contains eucalyptus fibers, which ensures that all used fibers show similar behaviour.

Only the fibers on the inside of a paper sheet were used since the outside of the paper sheet is treated to make the paper sheet flat and white. The inner

fibers can be reached by splitting the paper sheet with adhesive tape. Two pieces of tape were attached to both sides of the paper sheet and by pulling the two tapes away from each other the paper sheet gets split, see Figure 3-1. This method creates thin layers of inner fibers. Small pieces of these layers were gently pulled off by the use of a tweezer. Single fibers were sticking out at the edges of an extracted layer. The extracted layer with its fibers sticking out was then glued on a glass slide by the use of nail varnish, as shown in Figure 3-2. The nail varnish was placed on the extracted layer and on the end of the fibers which were sticking out. This creates several fibers which were fixed on both ends by the use of nail varnish. The nail varnish prevents the fibers from curling and twisting. In general, the extracted layer had a dimension of around 3 by 3 mm. The sticking out fibers had a width of approximately 30 μm and a length of 2 mm.
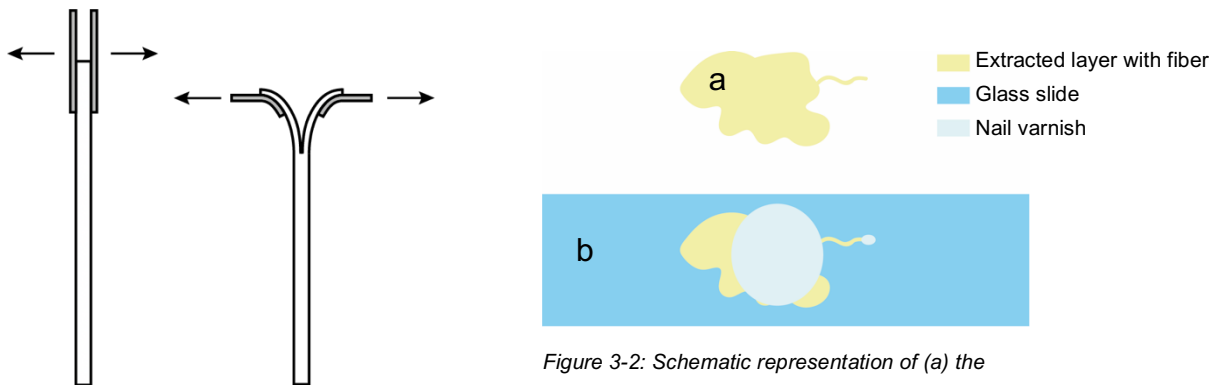
Figure 3-1: Splitting of a paper sheet with two pieces of adhesive tape, to get at the inner part of a paper sheet.

Figure 3-2: Schematic representation of (a) the extracted layer with a fiber sticking out, (b) the fixation of the sample on the glass slide.

After the sample has been prepared on a glass slide, the sample undergoes a patterning procedure. This was needed since a fiber has in general a relatively flat surface which is unfavorable for the Global Digital Height Correlations. Besides the flatness, the surface of the fiber can also change during different relative humidities, see for example the results of Lee et al. (Figure 2-15). For the patterning procedure an airbrush (vidaXL 141516) was used. First, the liquid solution was prepared. A solution of 5 mL ethanol with 50µL of silica particles with a size of 500 nm was sonicated for 5 minutes at a level of 9 at a temperature of 24°C. This sonication was to reduce the clustering of the particles inside the solution.

Secondly, the solution was poured in the airbrush and the sample was placed in the fume hood to prevent the inhalation of the particles. The airbrush was kept approximately 30 cm away from the sample which creates evaporation of the small ethanol droplets during spraying.

Finally, the spraying of the solution on the sample starts. Spraying was done at 1 bar. During spraying the trigger on the airbrush was not pulled backwards but only pressed (See figure A-3). This creates a spraying mist with an amount of liquid as low as possible. This was done to avoid any clustering of the liquid inside the mist. All the liquid was sprayed on the sample which took approximately 5 minutes.

When the first layer of 500 nm particles was applied the same procedure was used to create a layer of 1 μm particles.

As a result a thin layer of a combination of 500 nm particles and 1 μm particles was created, see Figure 3-3. See Appendix A, for the optimization of the patterning technique.

All the patterned fibers which were sticking out were scanned by the use of the Bruker NPFlex. The visibility of the fiber itself was important but also the pattern on the surface was important. A homogenous pattern of 500 nm and 1 μm particles was desired and sought on the fibers. The selection for the best and used fibers was done by hand.
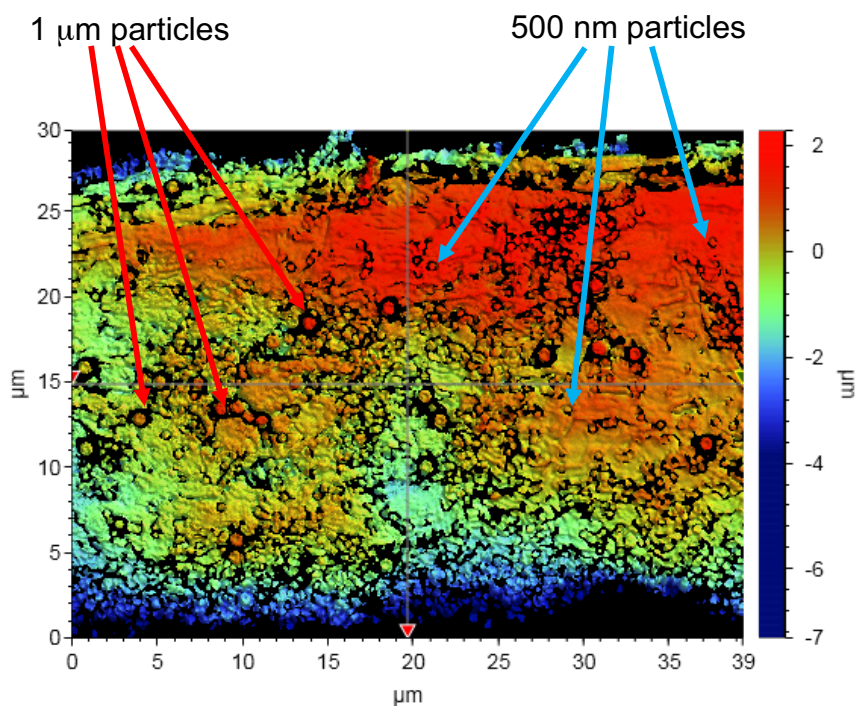
Figure 3-3: Fiber surface topology with a pattern of 1 μm and 500 nm particles

3.2   Climate control

The sample is kept in a climate box during the experiment. See Figure 3-4 for a schematic section view of the climate box. In this climate box the temperature and the relative humidity were regulated by a controller box. The controller box controlled the temperature by the use of a heating baseplate which was placed below the climate box. The heat is transferred from the baseplate to the walls of the climate box which results in a certain temperature inside the climate box. During the experiments the temperature was controlled at 23 °C. The relative humidity in the climate box was controlled by pumping in and out a mixture of dry nitrogen and humidified air. The mixing and the ratio of the mixture were done by the controller box itself. The climate box is a closed box with a top plate with a small hole. The sample is placed on a support pillar to lift the sample higher than the top plate. This is necessary since the used profilometer (Bruker NPFlex) has a turret with four lenses and

it is physically impossible to move one single lens through the hole without damaging the other lenses. Besides the humidity sensor (Sensirion SHT71) of the controller box a separate humidity sensor (Sensirion SHT2x) is attached to the small support pillar near the sample to obtain the data of the relative humidity and temperature near the sample in time. A silicone cone was placed over the sample and the humidity sensors to close the climate box between the lens and the top plate. A small plate was used to guide the humidified inlet air into the cone to make sure that the area around the sample achieves the correct environmental conditions.
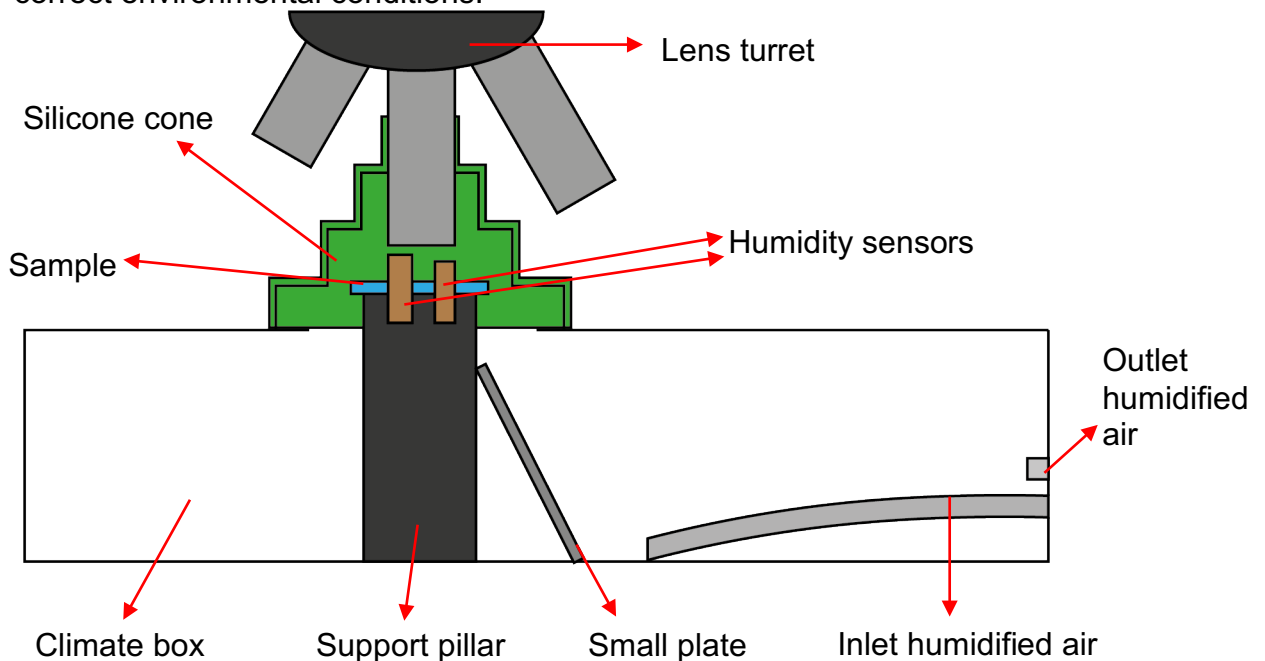
Figure 3-4: Schematic section view of the climate box.

In all the experiments the sample undergoes the same humidity program in time. First the sample is conditioned at 50% RH at 23°C for an hour. Subsequently the humidity is increased to 80% RH at 23°C at a rate of 10% RH/hour. After this increase the humidity is fixed at 80% for two hours to let the fiber relax.

3.3 Profilometry

The Bruker NPFlex is used to construct topology maps of the fiber surface, see for example Figure 3-5. Appendix B discusses the motivation for using this device and the optimization of its settings. The Bruker NPFlex works with vertical scanning interferometry (VSI). With this technique, light from a source is divided into two beams by a beam splitter. One beam reflects on a reference mirror and the other beam on the sample. The two beams are then recombined to create an interference pattern. The interference pattern is used to determine the difference in path length between the beams, which is used to determine the height distribution of the sample surface. The settings which can be set are the light source, the light intensity of the light source and the threshold. The threshold is a boundary which determines the amount of

reflected light which is used to create the topology image. The threshold and the light intensity are fiber dependent so every fiber can have slightly different settings. During the experiments a green light source is used since it results in better GDHC correlations (see Appendix B). This is probably due to the fact that green light uses one wavelength instead of multiple in the case of white light. The light intensity was automatically determined for every fiber by the software, since it turned out that the automatic determination of the light intensity by the software seems to results also in better GDHC correlations (see Appendix B). The threshold was set between 10% and 12%. This range was determined in an optimization step which is explained in Appendix C. The Bruker NPFlex made a scan of the fiber surface every minute with a magnification lens of 100x and an internal lens of 2x to obtain detailed topology patterns of the fiber surface. This lens combination reduces the field of view to 39.3 x 29.7 μm, for an example see Figure 3-3 and Figure 3-5.
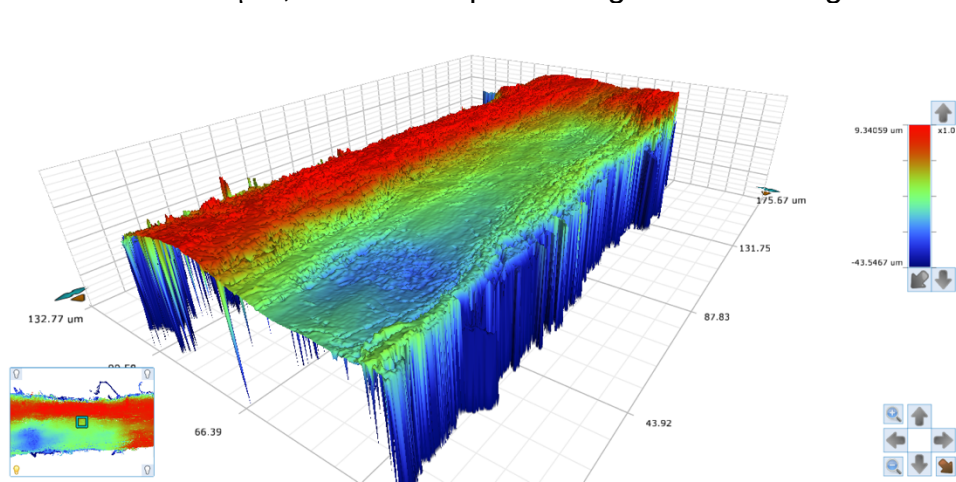

Figure 3-5: Topology image of a fiber surface. Settings: 50x magnification, threshold 2% and a green light source with an light intensity of 8%.

3.4   Settings for Global Digital Height Correlation

The working principle of Global Digital Height Correlation with its settings and terminology is explained in Section 2.4. The optimization of the settings can be found in Appendix C. During all the experiments in Chapter 4 the same settings were used, as listed in Table 3-1.

Setting:	Value:
Coarse grain step	No coarse graining
Convergence criterion	10^{-4} $\underline{\delta\lambda}$
Maximum iterations	500
Basis shape function	Polynomial
Order shape function	2nd
Masking	Used with a dilation of 2 rows around a NaN filled pixel.
Reconstructed data	Interpolation
Gradient	$\vec{G}_1 = \dfrac{\partial f}{\partial x_0}\vec{e}_x + \dfrac{\partial f}{\partial y_0}\vec{e}_y - \vec{e}_z$

Table 3-1: Optimized settings for the GDHC correlations.

The choice of the order of the shape function and its basis determine the kinematic freedom of the solution space. From the results of Bastawrous [8] a conclusion was made that the 4th order of the polynomial basis shape function would be sufficient. With this in mind the basis of the shape function was also chosen to be polynomial. The order of the shape function was determined from the results of different correlations which are described in Appendix C. From this we could conclude that a 1st order shape function would be sufficient. Since a fiber has an elliptical shape, membrane shaped deformations can occur as well and these deformations cannot be captured by the 1st order polynomial shape function. With that in mind, the order of the shape function was chosen to be 2nd order to capture also these membrane shaped deformations.

The masking feature was applied during the correlations of Chapter 4. The obtained mask was also dilated to avoid large residuals. Dilation of the mask is gained by masking single pixels around a NaN filled pixel. This dilation can be extended to 2 or even more rows of pixels around a NaN filled pixel. Figure 3-6 shows an example of the dilation of the mask feature.
The dilation of the mask was used for the following reasons:
- Topology images does not contain any information in the NaN filled pixels due to the transparency of the fiber in combination with the higher threshold which was used for creating robust residual fields. The obtained displacement around these pixels can introduce large errors.
- The masking function only works for the reference image f and not for the deformed image g. To exclude the NaN filled pixels in the deformed

image we used reconstructed data. The NaN filled pixels were interpolated to create an image without any NaN filled pixels. This interpolation affects the pixels around a NaN filled pixel.

- Since the edges of the small particles are relatively steep it is reasonably to avoid these areas. By 2x the dilatation of the mask the pixels around the particles are masked as well which excludes the steep edges of the particles.
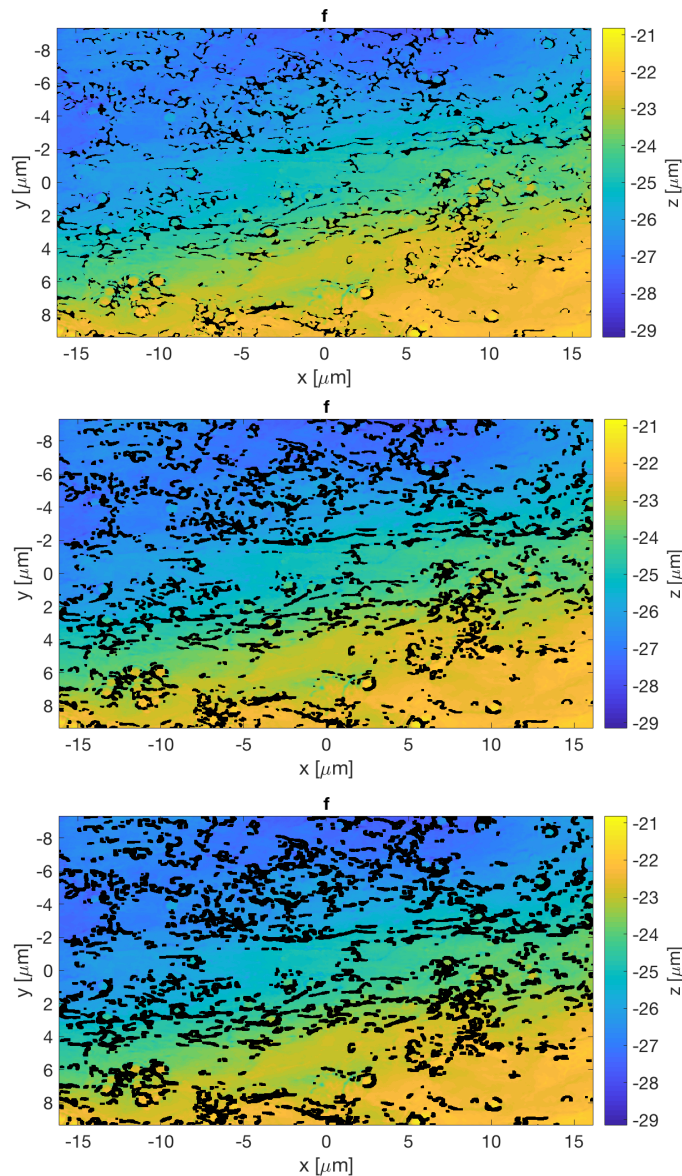

Figure 3-6: (a) Reference image f with NaN filled pixels (black pixels), (b) Reference image f with a dilatation of NaN filled pixels of 2 and (c) Reference image f with a dilatation of NaN filled pixels of 4.

The displacement fields from the GDHC are the projected displacement fields of the fiber surfaces. These projected displacement fields can be used to calculate the strain fields but it will not be representative since fibers can curl and twist during the experiment. The calculated projected strain fields can have large strains due to the curling and twisting of fibers. To avoid this, the surface strain fields, i.e. the strains along the fiber surface, need to be calculated [15]. The actual, surface, logarithmic strains are calculated with the stretch ratios:

$$\epsilon_{tt} = \ln(\lambda_t) \qquad\qquad (\,3.1\,)$$

$$\epsilon_{ll} = \ln(\lambda_l) \qquad\qquad (\,3.2\,)$$

where, λ_t and λ_l are the stretch ratios ($\lambda = \frac{current\ length}{original\ length}$) in the tangential ($\epsilon_{tt}$) and longitudinal directions (ϵ_{ll}), respectively, and given by:

$$\lambda_t = \frac{L_t^g}{L_t^f} \qquad\qquad (\,3.3\,)$$

$$\lambda_l = \frac{L_l^g}{L_l^f} \qquad\qquad (\,3.4\,)$$

L_t^g and L_t^f are denoted in Figure 3-7 and defined as:

$$L_t^g = \sqrt{(\Delta_x(x + u_x))^2 + (\Delta_x(Z_f + u_z))^2} \qquad\qquad (\,3.5\,)$$

$$L_t^f = \sqrt{(\Delta_x(x))^2 + (\Delta_x(Z_f))^2} \qquad\qquad (\,3.6\,)$$

where Z_f is the height map of the reference image f, while $\Delta_x(\cdot)$ denotes an operator that acts on a field to produce the finite difference of the field in the x-direction. A surface polynomial fit (5th order) of the reference image is used, since the reference surface is expected to be non-smooth due to the applied particle pattern. This surface fit will result in more smooth displacement fields. Furthermore, L_l^g and L_l^f are given by:

$$L_l^g = \sqrt{(\Delta_y(y + u_y))^2 + (\Delta_y(Z_f + u_z))^2} \qquad\qquad (\,3.7\,)$$

$$L_l^f = \sqrt{(\Delta_y(y))^2 + (\Delta_y(Z_f))^2} \qquad\qquad (\,3.8\,)$$

where $\Delta_y(\cdot)$ is the operator that produces the finite difference of the specified field in the y-direction.
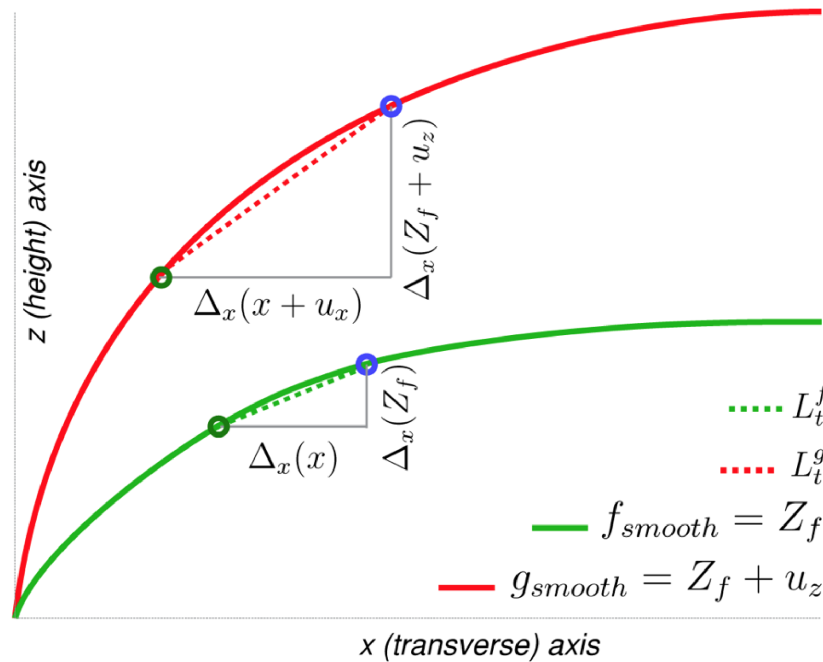

Figure 3-7: A schematic illustration of L_t^g and L_t^f, used for the determination of the surface transverse strain ϵ_{tt} [15].

The displacement fields are used to obtain the surface strain fields as described above. This will result in representative surface strain fields, Figure 4-2 represents the strain fields ϵ_{ll} and ϵ_{tt}. From the strain fields an average is taken to quantify the strain of a fiber at a specific relative humidity. This average is taken over a specific region of interest (yellow marked box in Figure 4-2) which excludes the sides of the displacement fields. These sides are less reliable because of the polynomial shape functions. These shape functions can largely fluctuate on the sides of the displacements fields. The size of this region of interest (yellow box) is 15 x 28.5 μm.

4   Results & Discussion

The method described in Chapter 3 was used to extract hygroscopic displacement and strains from fiber surfaces taken during changing relative humidity. This chapter starts with analyzing the obtained results before the actual accuracy of the method is determined which is finally compared with the work of Bastawrous.

4.1   Displacement and strain fields

As a result of the GDHC, at least 1200 displacement fields (X, Y and Z) are obtained for every fiber. Figure 4-1 represents the displacement fields of the correlation at 80% relative humidity for one fiber. The displacement fields in the three directions show different fluctuations over the entire fiber surface. For example, the displacements in the x-direction (horizontal) are all negative which means that the entire fiber moves to the left. The left side of the fiber surface moves 0.2 μm more to the left than the right side of the fiber surface which will result in a certain strain. The same kinematics can be seen for the displacements in the y-direction (vertical). In the z-direction the upper left corner moved -0.5 μm and the bottom right corner moved -0.9 μm in the out of plane direction which results in a tilted kinematics. This tilt in the z-direction confirms the earlier mentioned kinematics (curling and twisting) of fibers due to change in relative humidity. Hence, using the displacement fields, the entire kinematics of the single fiber can be visualized.
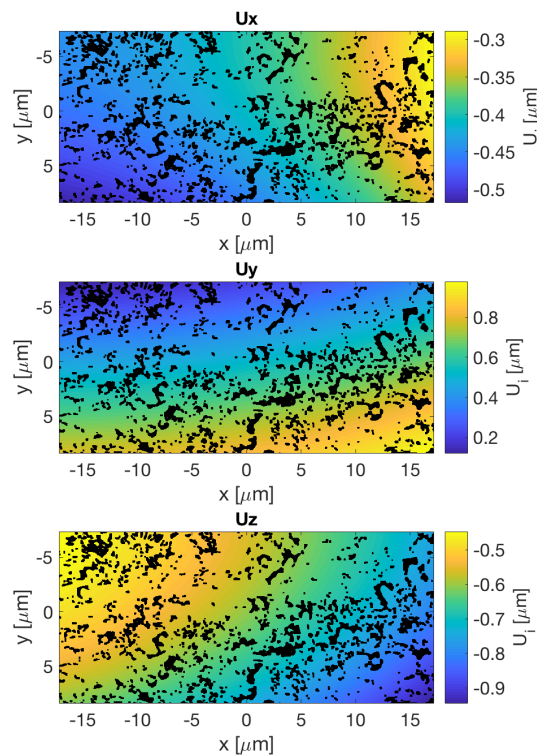
Figure 4-1: Displacement fields in x-, y- and z-direction of a single fiber after a humidity step from 50% to 80% relative humidity.

All the displacement fields are used to obtain the surface strain fields as described in Section 3.4. Figure 4-2 represents the strain fields obtained from the previous displacement fields (Figure 4.1). As mentioned earlier the yellow marked box is the area which was used for calculating the average strain. The ϵ_{ll} strains are the strains in the longitudinal direction and the ϵ_{tt} strains are the strains in the transverse direction. The longitudinal strain field ϵ_{ll} shows a small gradient from left to right. The strain field shows the expected strain since the displacement field in the x-direction also has a gradient from left to right. The gradient in the displacement field on the right side is higher than on the left side which creates the expected larger strain of 0.005 in the right side and a lower strain of 0.0008 in the left side of the fiber surface.
The transverse strain field ϵ_{tt} shows also a small gradient but this gradient goes from top to bottom of the fiber surface. The strains in the top region of the yellow box are approximately 0.04 and the strain at the bottom region of the yellow box are approximately 0.03. In general, the strains in the transverse direction are larger than the strains in the longitudinal direction. This outcome is not surprisingly since in general the strains in the transverse direction of a fiber are larger due to structure of the fiber, and due to the boundary conditions of the sample preparation (gluing).
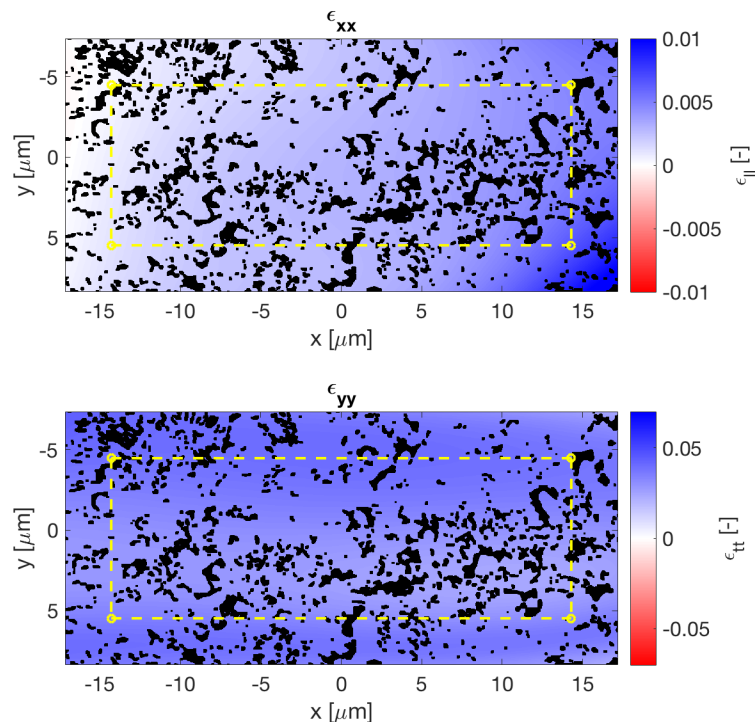
Figure 4-2: Strain fields in Longitudinal direction (ϵ_{ll}) and transverse strain (ϵ_{tt}).

4.2   Strains for relative humidity step (50%→80% RH)

To obtain the strains at different relative humidities, the average strains have been extracted from the yellow marked box in the strain fields (see for example Figure 4.2) for the longitudinal and transverse strains, see Figure 4-3 for the results. The fluctuations of the strains between the different fibers can originate from the fiber structure, dimensions of the fiber and the deformation history from papermaking. Also, the preparation of the fiber sample can have an influence on the strains since the fibers are glued on the glass slide by hand. This creates a large variation between the kinematic freedom for different fiber samples which results in different strains. The transverse strains ϵ_{tt} varies between 0.025 and 0.04 while the longitudinal strains ϵ_{ll} varies between -0.0001 and 0.003 for the three tested paper fibers.

For strains in transverse and longitudinal direction it applies that the slope of the increased strain is much higher for higher relative humidities than for lower relative humidities. A negative longitudinal strain ϵ_{ll} is noticeable for fiber 1, which is remarkable because the moisture content of the fiber increases due to an increased relative humidity but the longitudinal dimension is decreasing. Lee et al. [7] discovered also the same remarkable deformation for fibrils. Lee et al. stated that these dimensional changes can be attributed to a rearrangement of the internal fibrils. One explanation was that the moisture content is weakening the bonds between the individual mircofibrils. This increases the freedom of movement and allows the fibrils to rearrange into a lower energy state. Another explanation was that defects occur at discrete locations along the length of the fiber. Due to the moisture content uptake these defects will swell. The internal fibril chains must travel an arced path around these defects, which is longer. As a result, the internal fibril chains extending along the length of the fiber appear to contract and cause the fiber to shrink when water is taken up.

Noticeable is the scatter of the obtained strain data. Larger scatter of the strains is visible for the transverse strains ϵ_{tt} compared to the longitudinal strains ϵ_{ll}. The reason for this difference in scatter is discussed later in Section 4.3.

Another interesting phenomenon is the increased strain at a constant relative humidity. This is likely due to the relaxation time of the fiber, which seems to be in longer than 2 hour, see Figure 4-5 below, which shows the strains of a fiber in time for a cyclic relative humidity. When the relative humidity is kept constant at 80% relative humidity the strains still increased in time.

The obtained strains in Figure 4-3 are smaller than the strains mentioned by Niskanen [1]. Niskanen concluded that over the range of humidity of 0-100%, a fiber can expand by about 1% in the longitudinal direction and by about 20-30% in the transverse direction. This can be explained by the relative humidity range, Niskanen used a range of relative humidity of 0-100% and for our experiments the range of relative humidity is 50-80%. Another reason for the difference can come from the sample preparation. As mentioned earlier the fibers are glued on a glass slide by hand which creates a restriction on the

kinematic freedom of the fiber. This can eventually result in smaller hygroscopic strains. On average, the transverse strain ϵ_{tt} is 22 times larger than the longitudinal strain ϵ_{ll}. This is a comparable ratio with the results of Niskanen. The magnitudes of the strains and the strain curves are in line with the results in the literature, see the results of Yamamoto et al. [6], Nanko and Wu [8] and Bastawrous [12] which are described in Section 2.3. From this we can assume that the results are reliable and useful.
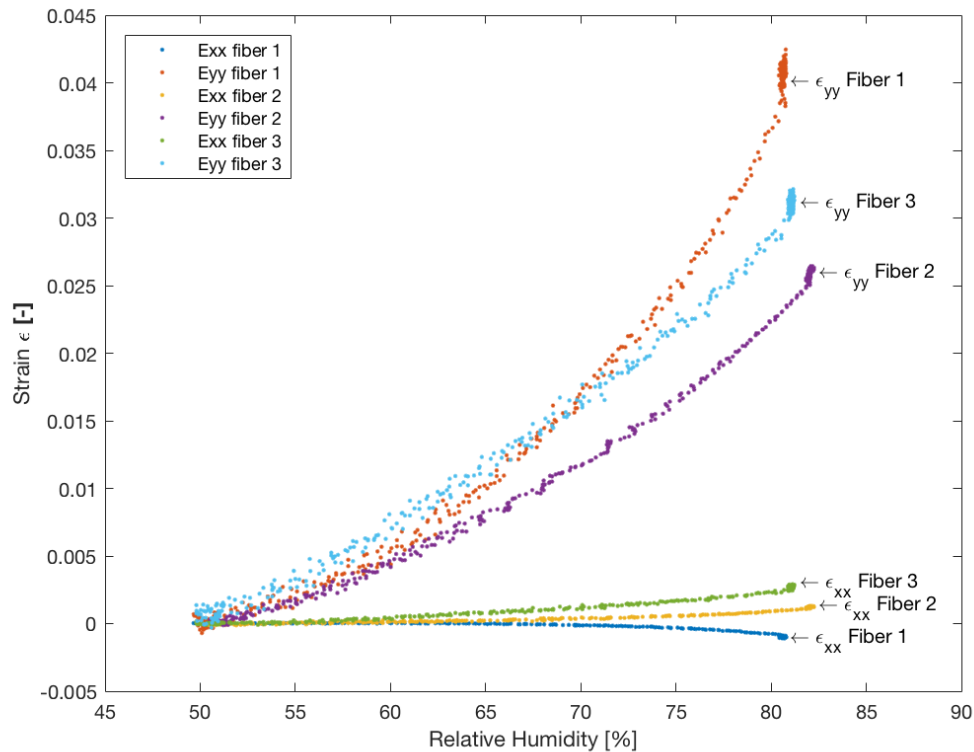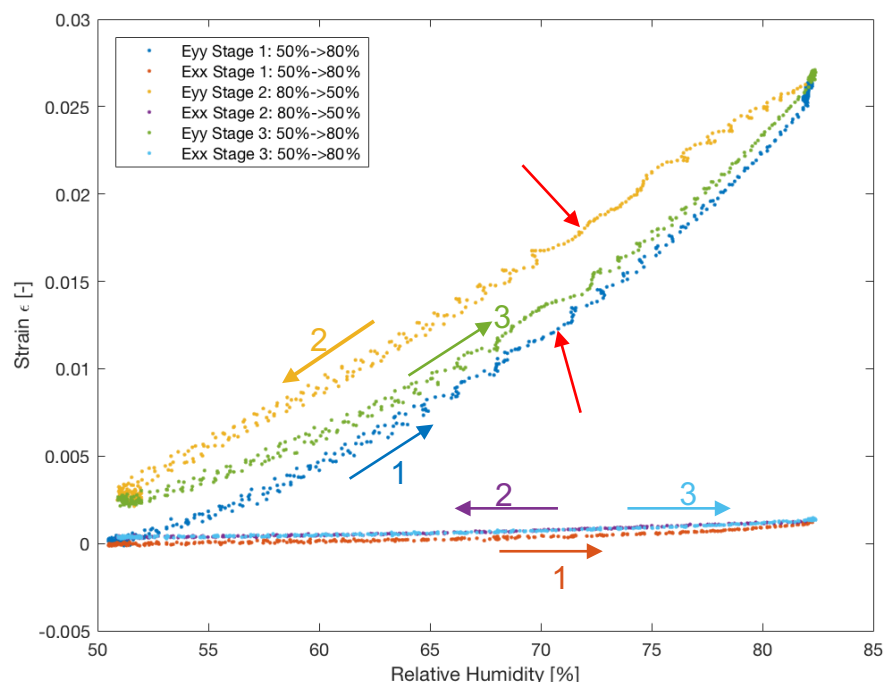

Figure 4-3: Longitudinal strains (ϵ_{ll}) and transverse strain (ϵ_{tt}) versus relative humidity for three different paper fibers.

4.3 Strains for relative humidity cycle (50%→80%→50%→80% RH)

Besides the single relative humidity step from 50% to 80% also a cyclic relative humidity experiment was conducted in three stages. Stage 1: the relative humidity was changed from 50% to 80% in 3 hours, then the 80% relative humidity was kept constant for 2 hours. Stage 2: the relative humidity was changed from 80% back to 50% in 3 hours, then the 50% relative humidity was unchanged for 2 hours. Stage 3: the relative humidity was again changed from 50% to 80% in 3 hours, then the 80% relative humidity was unchanged for 2 hours. See Figure 4-4 for the strains in longitudinal and transverse direction during the cyclic humidity experiment. As can be seen, the relative humidity range is not between 50% to 80% but from 50% to 82%. This difference is due to the different humidity sensors. As mentioned earlier, one humidity sensor is connected to the controller box where the relative

humidity was set between 50% and 80% and the other humidity sensor was used to extract the humidity data. Both humidity sensors were placed at the same position in the climate box.

Noticeable is the decreasing and increasing transverse strain ϵ_{tt} during constant relative humidities of 50% and 80%. Figure 4-5 represents the longitudinal and transverse strain in time. As mentioned earlier, when the relative humidity is kept constant at 80% the transverse strain (ϵ_{tt}) still increases slightly and when relative humidity is kept constant at 50% the strain decreases slightly, see Figure 4-5. As mentioned earlier, this increase and decrease is probably due to the relaxation of the fiber. The fiber still deforms even after 2 hours of relaxation time.

Another remarkable phenomenon is the scatter of the transverse strain ϵ_{tt} in stage 1, 2 and 3 in the relative humidity. This scatter probably occurs due to the fluctuations of the relative humidity during the experiment, see Figure 4-6. In the relative humidity range of 50% to 65% large fluctuations in the relative humidity appears which causes large fluctuations in the transverse strain. In the range of 65% to 75% relative humidity, fluctuations of the relative humidity and the scatter of the transverse strain are decreased significantly, where the smoother curves clearly exposes the trend in the data (red arrow marked areas in Figure 4-4 and the marked areas in Figure 4-6). Fluctuations in the relative humidity and scatter of the transverse strain reappears in the relative humidity range of 75% towards 80%. This strain scatter is lower than the strain scatter in the relative humidity range of 50% to 65% due to smaller relative humidity fluctuations.

These relative humidity fluctuations seem to be the main reason for the earlier observed larger scatter of the strain of the transverse strain ϵ_{tt} compared to the longitudinal strain ϵ_{ll} in Section 4.2. This could be explained by the higher strain level of the transverse strain which causes the large scatter in the transverse strain data.

Figure 4-4: Longitudinal strains (ϵ_{ll}) and transverse strain (ϵ_{tt}) versus relative humidity for three different paper fibers. The arrows mark the areas were less scattering of the strain data occurs.
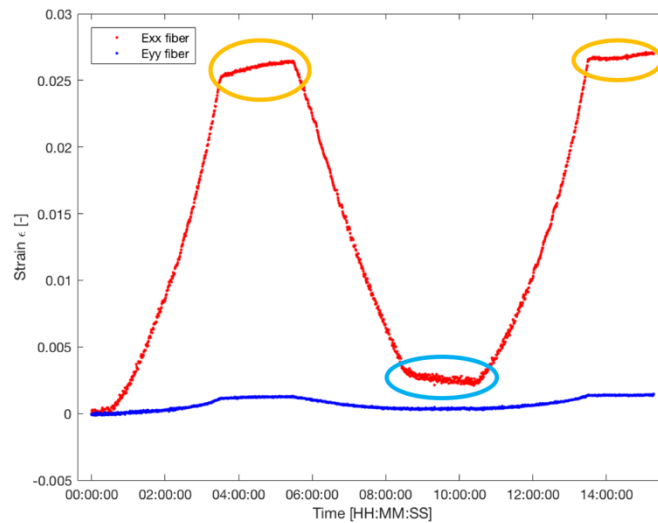
Figure 4-5: Longitudinal (ϵ_{ll}) and transverse (ϵ_{tt}) strain in time for a cyclic experiment. (50%-80%-50%-80% RH). Marked areas are the transverse strains at 80% RH and at 50% RH.
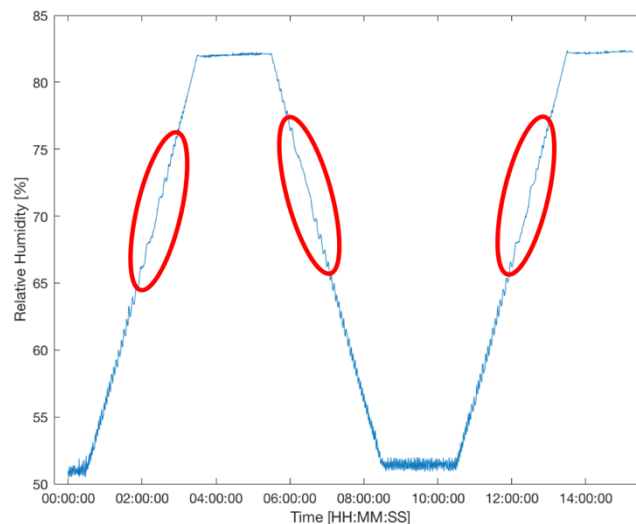

Figure 4-6: The relative humidity in time during the cyclic experiment. The marked areas are the relative humidities between 65% and 75% were the fewest fluctuations occur.

During stage 1 (50%→80% RH) the fiber undergoes a longitudinal strain ϵ_{ll} of 0.001 and a transverse strain ϵ_{tt} of 0.026. The discussion about this part of the strain curve has already been done in Section 4.2.

During stage 2 (80%→50% RH) the fiber undergoes a decrease in longitudinal strain ϵ_{ll} of 0.001 and a decrease in transverse strain ϵ_{tt} of 0.023. At the range of 80% to 75% RH the transverse strain decreases with a smaller slope compared to the slope in the same range of RH in stage 1. From 75% to 50% RH the slope in stage 1 and 2 are similar. At the end of stage 2, the fiber does not return to its initial state when it is conditioned again at 50% relative humidity; there is a positive residual longitudinal strain ϵ_{ll} of around 0.0004 and a residual transverse strain ϵ_{tt} of around 0.002. These residual strains are probably due to a hysteresis effect since the fiber is returned from a higher

to a lower relative humidity state. The amount of moisture content is probably not the same as at the initial state.

In literature, Bastawrous also performed a cyclic experiment and the residual longitudinal strain was 0.006 and the residual transverse strain was 0.002. The residual longitudinal strain is 5x larger than the residual longitudinal strain obtained during the experiments in this project. This is most likely due to the sample preparation which creates a large difference in kinematic freedom. However, the residual transverse strain is the same as the residual transverse strain obtained by Bastawrous.

During stage 3 (50%→80% RH) the fiber undergoes again an increase in longitudinal strain ϵ_{ll} and transverse strain ϵ_{tt}. At the range of 50%→65% RH the transverse strain increases with a smaller slope compared to the slope in the same range of RH in stage 1 and 2. From 65%→80% RH the slope in stage 3 and 1 are similar. On the end of stage 3, the fiber seems to undergo an increased longitudinal and transverse strain compared to the strains on the end of stage 1. On the end of stage 3 the longitudinal strain ϵ_{ll} is 0.001 which is higher than the strains on the end of stage 1. The transverse strain is 0.027 which is 0.001 higher than the strain on the end of stage 1. Also in this case a hysteresis effect occurs. The fiber at the end of stage 3 probably contains more moisture than the fiber at the end of stage 1.

Conclusions about the underlying physics for these residual strains after stage 2 and 3 should be cautiously taken. The actual moisture content of the fiber should be known in order to determine if the fiber has truly returned to its initial or previous moisture content.

4.4 Comparison Bastawrous

In the work of Bastawrous a fiber was conditioned at a range of 15% to 90% relative humidity. Bastawrous extracted for every obtained strain field the strain of a particular point in the middle of the strain field. All the extracted strains were averaged at specific relative humidities. Eventually, 10 transverse and longitudinal strain data points were obtained and used for analysis.
All data results of Bastawrous and the experiments are fitted with a smoothing spline to visualize the trend of the data points. The fit is chosen in a way that it represents the individual data points well with a continuous curve without small fluctuations, see Figure 4-7 and Figure 4-8.
The obtained strains of Bastawrous [8] show a similar trend as observed in the data from the experiments. Namely, the slope of the increased strain is much higher for higher relative humidities than for lower relative humidities. The longitudinal strain ϵ_{ll} at 80% relative humidity is at least 4 times larger than those measured in this project, see Figure 4-7. The large difference in longitudinal strain may be due to the properties of the used fibers. Another explanation is the sample preparation which influences the kinematic freedom of the fibers.
The transverse strain ϵ_{tt} curves are more similar, see Figure 4-8. The transverse strain ϵ_{tt} at 80% RH are 0.02 in the case of Bastawrous while the transverse strains for the three fibers tested are 0.04, 0.03 and 0.025. Between 50% and 80% relative humidity, the transverse strain curve of Bastawrous shows a similar trend as fiber 2. This already indicates that the results in the transverse direction are more comparable than the strains in the longitudinal direction.
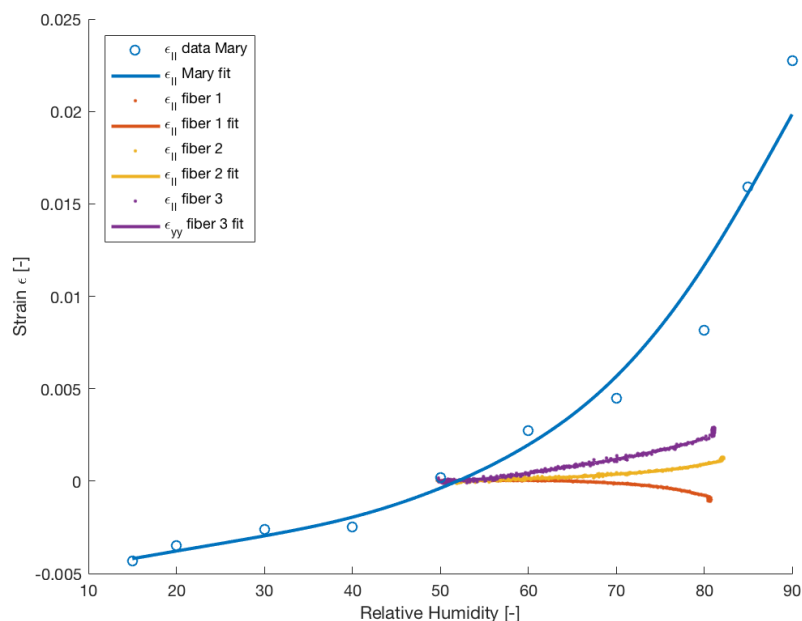
Figure 4-7: Longitudinal strains (ϵ_{ll}) versus relative humidity for three tested paper fibers and the fiber tested by Bastawrous [8].
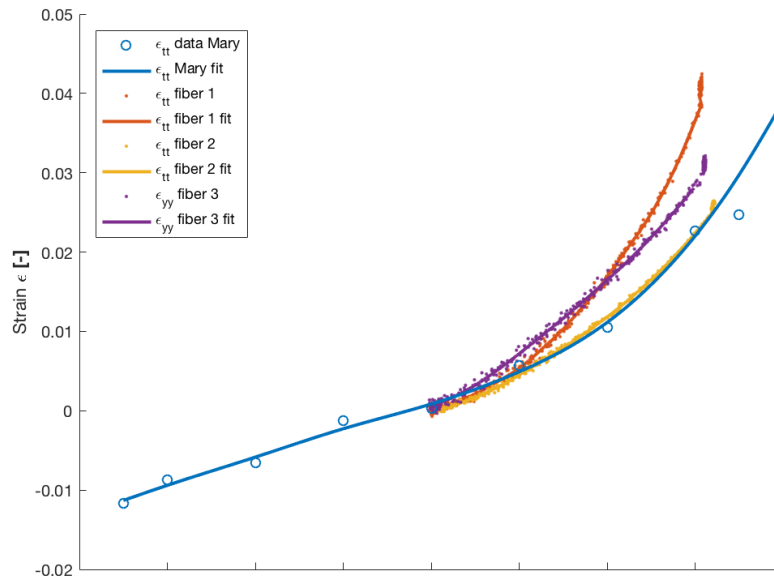
Figure 4-8: Transverse strains (ϵ_{tt}) versus relative humidity for three tested paper fibers and the fiber tested by Bastawrous [8].

Bastawrous calculated the accuracy of the used methodology by determining the 95% confidence interval for the measured strains at 15%, 50%, 85% and 90% relative humidity. Bastawrous mentioned that the 95% confidence interval was calculated with a total sample size of 31 and a t-distribution curve in transverse and longitudinal direction. Due to an incomplete explanation of the exact calculation, we assume that the mentioned confidence intervals of Bastawrous (see Table 4-1) are averages of the individual confidence intervals at 15%, 50%, 85% and 90% relative humidity in the transverse and longitudinal direction.

To determine the accuracy of the proposed optimized methodology the same procedure is used. A t-value of 2.042 (which is obtained from the t-distribution table) is needed for calculating a confidence interval of 95% with a sample size of 31. The confidence interval is calculated at a relative humidity of 50% and 80% for the longitudinal strains and transverse strains. Two approaches were used to calculate the confidence interval.

- Approach 1: The obtained strains in Section 4.2 were used for calculating the confidence interval. Worth nothing, these strains are the average strains of a region of interest of the strain fields (described in Section 3.4)
- Approach 2: Strains of a specific point in the middle of the strain fields are used for the confidence intervals. This approach is similar as the approach used by Bastawrous.

For both approaches the strains increases at a constant relative humidity of 50% and 80%, which was also observed in Section 4.2 and 4.3. To calculate the mean of these strains, which is used for standard deviation, a 1st order polynomial fit is used which represents the mean of the 31 strain samples. So, the standard deviations of the strains are calculated towards the polynomial fit.

Table 4-1 represents the confidence intervals for the three tested fibers during this project, determined with approach 1 and 2. Also the confidence intervals from Bastawrous are mentioned in the table. Approach 1 results in confidence intervals for the longitudinal strains ϵ_{ll} and transverse strain ϵ_{tt} which are

approximately equal to the confidence intervals calculated with approach 2. So, the approach for calculating the confidence intervals has no influence on the actual confidence interval. This is reasonable since with approach 1 strain fluctuations in the strain fields are averaged. While in approach 1 the strains are used from one single point in the strain fields.

Both approaches generate a confidence interval for the longitudinal strain ϵ_{ll} which is approximately 7x smaller than the transverse strain ϵ_{tt}. This is probably due to the elliptical shape of the fiber in the transverse direction. Since the fiber is relatively flat, looking in the longitudinal direction, the surface strain calculations will produce less noise compared to the more elliptical shaped transverse direction. Eventually this will also introduce more strain scatter in the transverse direction than in the longitudinal direction. Bastawrous obtained a 95% confidence interval of $2.30 \cdot 10^{-3}$ and $5.95 \cdot 10^{-4}$ in longitudinal and transverse direction. The proposed optimized methodology results in a 95% confidence interval of $1.47 \cdot 10^{-5}$ and $9.89 \cdot 10^{-5}$ in longitudinal and transverse direction. These confidence intervals are visualized in Figure 4-7 and Figure 4-8. Comparing the confidence intervals, results in an improvement in the confidence intervals of 150x in the longitudinal direction and 6x in the transverse direction. Looking at the strain data points and the confidence intervals we can conclude that the optimized methodology can be used to obtain more consistent and more accurate strain results compared with the methodology of Bastawrous.

		Approach 1: Average strain field			Approach 2: Single point in strain field		
		50% RH	80% RH	Mean	50% RH	80% RH	Mean
Fiber 1	ϵ_{ll}	$7.75 \cdot 10^{-6}$	$7.32 \cdot 10^{-6}$	$\underline{7.54 \cdot 10^{-6}}$	$6.86 \cdot 10^{-6}$	$6.53 \cdot 10^{-6}$	$\underline{6.70 \cdot 10^{-6}}$
	ϵ_{tt}	$1.26 \cdot 10^{-4}$	$1.36 \cdot 10^{-4}$	$\underline{1.31 \cdot 10^{-4}}$	$1.20 \cdot 10^{-4}$	$1.36 \cdot 10^{-4}$	$\underline{1.28 \cdot 10^{-4}}$
Fiber 2	ϵ_{ll}	$1.90 \cdot 10^{-5}$	$7.44 \cdot 10^{-5}$	$\underline{1.32 \cdot 10^{-5}}$	$1.85 \cdot 10^{-5}$	$7.46 \cdot 10^{-6}$	$\underline{1.29 \cdot 10^{-5}}$
	ϵ_{tt}	$4.40 \cdot 10^{-5}$	$2.10 \cdot 10^{-5}$	$\underline{3.25 \cdot 10^{-5}}$	$4.50 \cdot 10^{-5}$	$2.04 \cdot 10^{-5}$	$\underline{3.27 \cdot 10^{-5}}$
Fiber 3	ϵ_{ll}	$2.10 \cdot 10^{-5}$	$2.10 \cdot 10^{-5}$	$\underline{2.10 \cdot 10^{-5}}$	$2.41 \cdot 10^{-5}$	$2.48 \cdot 10^{-5}$	$\underline{2.45 \cdot 10^{-5}}$
	ϵ_{tt}	$1.60 \cdot 10^{-4}$	$1.33 \cdot 10^{-4}$	$\underline{1.47 \cdot 10^{-4}}$	$1.43 \cdot 10^{-4}$	$1.29 \cdot 10^{-4}$	$\underline{1.36 \cdot 10^{-4}}$
Bastawrous	ϵ_{ll}	x	x	x	x	x	$\underline{2.30 \cdot 10^{-3}}$
	ϵ_{tt}	x	x	x	x	x	$\underline{5.95 \cdot 10^{-4}}$

Table 4-1: Confidence intervals of Bastawrous [8] *and the confidence intervals of the obtained experiments in this project.*
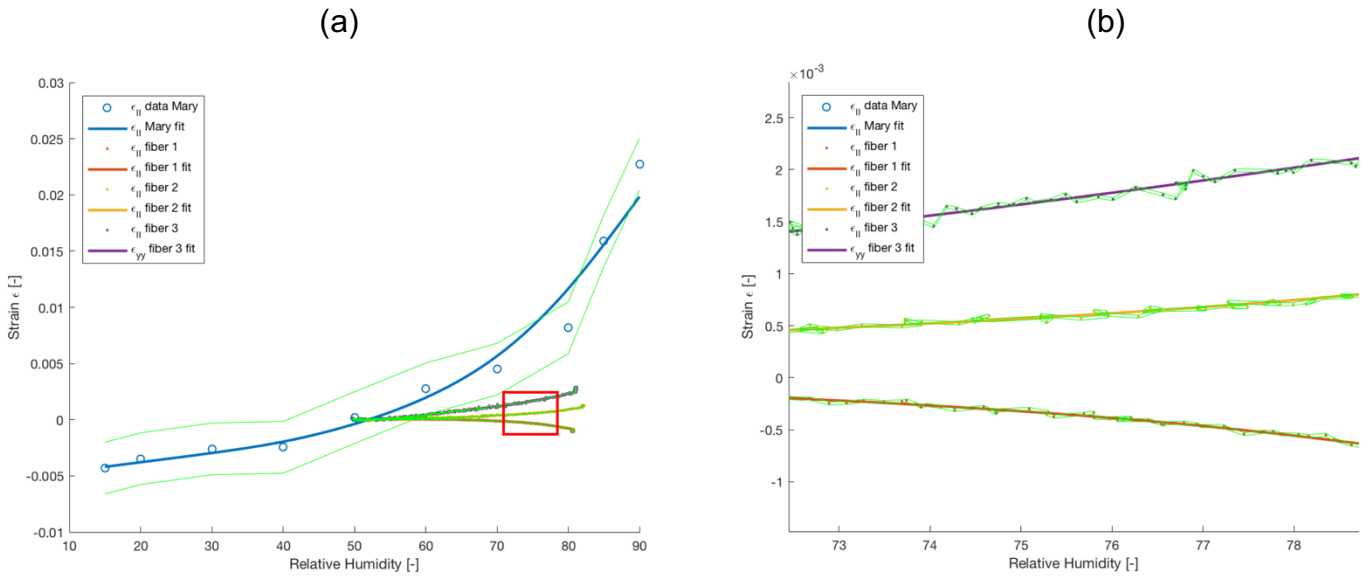
(a)

(b)

Figure 4-9: (a) Longitudinal strains (ϵ_{ll}) versus relative humidity for three tested paper fibers and the fiber tested by Bastawrous [8] with the confidence intervals. (b) Zoom of the red rectangular area.
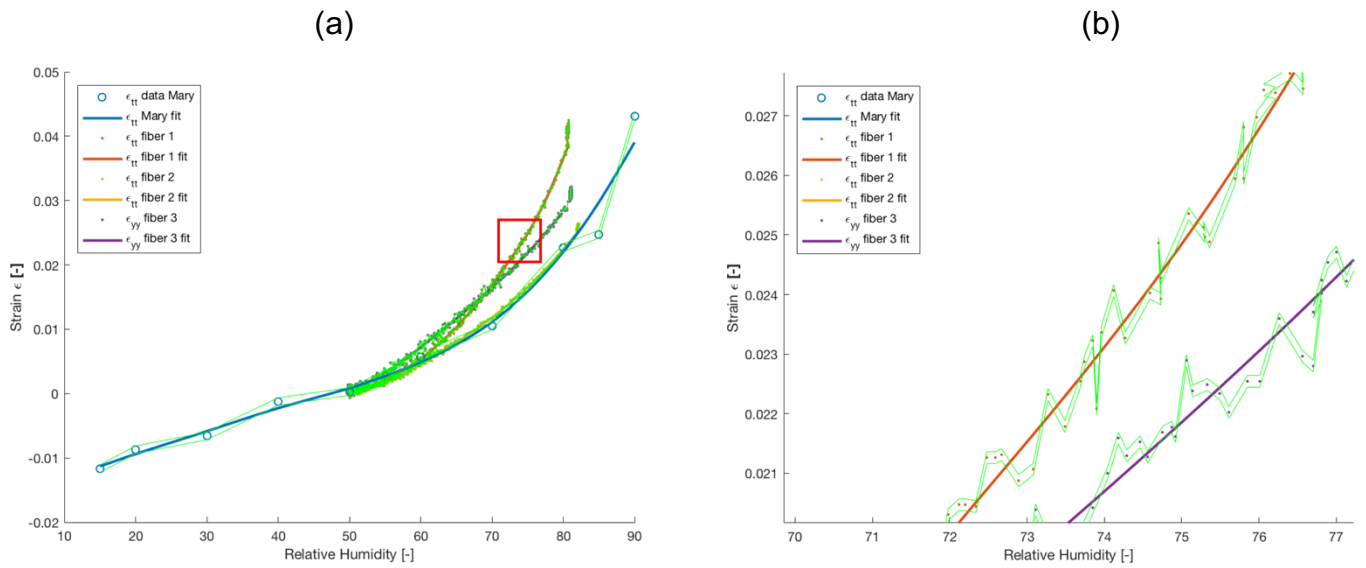
(a)

(b)

Figure 4-10: (a) Transverse strains (ϵ_{tt}) versus relative humidity for three tested paper fibers and the fiber tested by Bastawrous [8] with the confidence intervals. (b) Zoom of the red rectangular area.

5   Conclusions and recommendations

In this work, a methodology is developed, optimized and described to extract full-field measurements of displacements on a single fiber surface. Vertical Scanning Interferometry was used to produce fiber topographies at different relative humidities. Since fiber surfaces are in general relatively flat and can change during different relative humidities, nano particles were sprayed on the fiber surface to create topology features which are useful during Global Digital Height Correlations (GDHC). GDHC was used to analyze the obtained topologies and extract the displacement fields. Masking and creation of reconstructed data was needed since the fiber topologies included NaN filled pixels due to the transparency of the fiber in combination with the higher threshold which was used for creating robust residual fields. Dilatation of the mask was necessary to mask also the pixels around a NaN filled pixel and to avoid the steep edges of the particles on the fiber surface. 2nd order polynomial shape functions were used for the correlations since they can describe the kinematics of the fiber under changing relative humidity conditions. The optimized methodology has been successfully used to extract full-field displacements and strains from experimentally measured paper fiber topologies. The obtained average longitudinal strain ϵ_{ll} of 0.001 and the transverse strain ϵ_{tt} of 0.0325 during a relative humidity step of 50% towards 80%, lie in the strain range as described in literature.

Finally, the optimized methodology is compared with the work of Bastawrous [8]. The strain results from the optimized methodology and the results of Bastawrous are fitted with a smoothing spline to visualize the trend of the data points. The longitudinal strains of Bastawrous are significant larger than the obtained longitudinal strains from the experiments. This difference in longitudinal strain may be due to the properties of the used fibers. Another explanation could be the difference in kinematic freedom of the glued fibers. The transverse strain curve of Bastawrous is more similar than the transverse strain curves of the experiments. The optimized methodology results in a 95% confidence interval of 1.47·10^{-5} and 9.89·10^{-5} in longitudinal and transverse direction which is an improvement of the confidence intervals of 150x in the longitudinal direction and 6x in the transverse direction compared to the methodology of Bastawrous. Looking at the strain data points and the confidence interval we can conclude that the optimized methodology can be used to obtain more consistent and more accurate strain results compared with the methodology of Bastawrous.

Further improvements of the methodology can be found in the preparation of the samples. The fibers in this work are glued on a glass slide by hand. This can create a large variation in deformation freedom of the fibers which results in strain differences between different fibers. An improvement of the climate box is desirable since the fluctuations of the relative humidity have significantly influences on the obtained strains of the fiber. For a better understanding of the hygroexpansion of a fiber the moisture content of the fiber needs to be measured during the experiments.

6   Bibliography

[1]   K. Niskanen, *Paper Physics*. Helsinki: Finnish Paper Engineers'
         Association and TAPPI, 1998.

[2]   A. Kulachenko, *Mechanics of paper products*. Berlin: Walter de Gruyter
         Incorporated, 2011.

[3]   E. Bosco, M. V. Bastawrous, R. H. J. Peerlings, J. P. M. Hoefnagels,
         and M. G. D. Geers, "Bridging network properties to the effective hygro-
         expansivity of paper: experiments and modelling," *Philos. Mag.*, vol. 95,
         no. 28–30, pp. 3385–3401, 2015.

[4]   B. A. Meylan, "The influence of microfibril angle on the longitudinal
         shrinkage-moisture content relationship," *Wood Sci. Technol.*, vol. 6, no.
         4, pp. 293–301, 1972.

[5]   H. Yamamoto, F. Sassus, M. Ninomiya, and J. Gril, "A model of
         anisotropic swelling and shrinking process of wood," *Wood Sci.
         Technol.*, vol. 35, no. 1–2, pp. 167–181, 2001.

[6]   H. Nanko and J. Wu, "Mechanisms of paper shrinkage during drying,"
         Int. Pap. Phys. Conf., pp. 103–113, 1995.

[7]   J. M. Lee, J. J. Pawlak, and J. A. Heitmann, "Longitudinal and
         concurrent dimensional changes of cellulose aggregate fibrils during
         sorption stages," *Mater. Charact.*, vol. 61, no. 5, pp. 507–517, 2010.

[8]   M. V. Bastawrous, R. H. J. Peerlings, J. P. M. Hoefnagels, and M. G. D.
         Geers, "Direct Quantitative Measurement of Fiber Surface
         Hygroexpansion using Quasi-3D Digital Image Correlation," pp. 1–15.

[9]   M. V. Bastawrous, "A Multiscale Study of the Hygroscopic induced
         dimensional changes in Paper – Literature Review," 2014.

[10]   T. Joffre, *Structure and Mechanical Behaviour of Wood-Fibre
         Composites*. 2014.

[11]   J. M. Lee, J. A. Heitmann, and J. J. Pawlak, "Technique for the
         measurement of dimensional changes of natural microfibril materials
         under variable humidity environments," *Mater. Sci. Eng. A*, vol. 445–
         446, pp. 632–640, 2007.

[12]   A. Ruybalid, "Introduction to Digital Image Correlation," *Intern. Doc.
         Eindhoven Univ. Technol.*, 2013.

[13]   J.G.P. Neggers, "Ductile Interfaces in Stretchable Electronics," 2013.

[14]   J. Neggers, B. Blaysat, J. P. M. Hoefnagels, and M. G. D. Geers, "On
         image gradients in digital image correlation," *Int. J. Numer. Methods
         Eng.*, vol. 105, no. 4, pp. 243–260, 2016.

[15]   S. Shafqat, J. Hoefnagels, O. Van Der Sluis, and M. Geers, "A novel
         bulge test based characterization methodology for buckled membranes,"
         no. ESMC, pp. 6–7, 2015.

[16]   R. J. Lang, "Ultrasonic Atomization of Liquids," *J. Acoust. Soc. Am.*, vol.
         34, no. 1, pp. 6–8, 1962.

[17]   R. C. Neagu, E. K. Gamstedt, S. Bardage, and M. Lindström,
         "Ultrastructural features affecting mechanical properties of wood fibres,"
         Wood Mater. Sci. Eng., vol. 1, no. 3, pp. 146–170, 2006.

Appendix A: Optimization of the patterning of single fiber surfaces

In general fibers have a very flat surface, see Figure A-1 and Figure A-2. Besides the flatness also the fiber surface can change due to a change in moisture content. This change of fiber surface is described Section 2.2. GDHC tracks topology features on a fiber surface during the correlation procedure to determine the displacements and strain fields. Since the fibers are very flat and the present topology features can change or even disappear during changed relative humidity, the fiber surface needs externally applied pattern features.
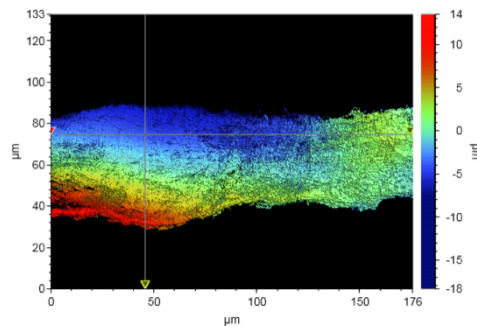
Figure A-1: Topology image of a paper fiber without particle pattern.
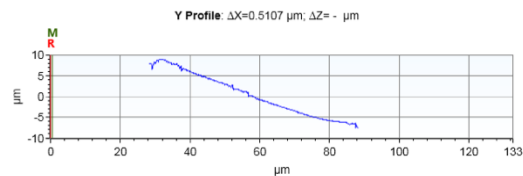
Figure A-2: Y-profile (vertical) from the topology image on the left.

Working principle of two patterning methods

Two different techniques have been developed and optimized during the project. Method 1 makes use of a humidifier (Beurer LB12) and method 2 makes use of an airbrush (vidaXL 141516).

Method 1 works as follows.
Inside the humidifier a piezoelectric transducer is immersed in a liquid solution. The liquid solution consists of a liquid and individual particles. These particles can come from powders or purchased microspheres. The transducer converts a high frequency, electronic signal into a high frequency (ultrasonic) mechanical oscillation. The frequency of the humidifier is 1,7 MHz. The liquid solution tries to follow the mechanical oscillations but because of the ultrasonic high frequency this is not possible. Tiny droplets are smashed out of the liquid solution and are dissipated into the air. Some of the droplets contain particles. These small droplets form a vapor which are blown away with an air flow. The particle pattern is created by blowing this vapor on the sample.

Method 2 makes use of an airbrush gun. Airbrush guns are normally used in the art industry. Figure A-3 represents a section view of an airbrush gun. The airbrush gun works with an active airflow and a liquid solution, normally paint. The air which is escaping around the tip of the airbrush forms a vacuum that pulls paint out of the tip which forms the spray pattern (see Figure A-4). By moving the needling backwards or forwards with the trigger more or less paint can be pulled out by the air. In the experiments a liquid solution of ethanol with microsphere particles is used instead of paint.
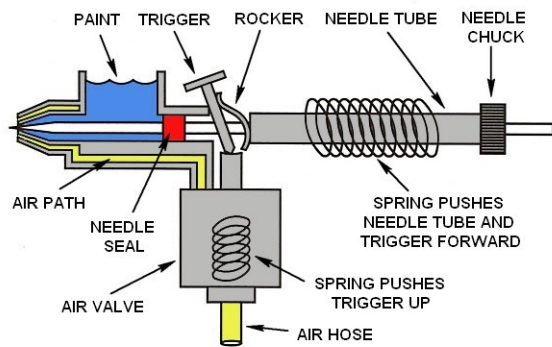
Figure A-3: Schematic section view of an airbrush gun.
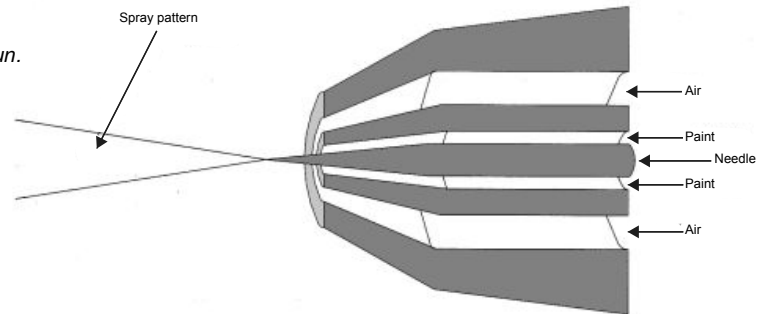
Figure A-4: Schematic section view of the tip of an airbrush gun.

Experiments with the patterning methods

Method 1: experiment 1
This setup, which is represented in Figure *A-5*, uses the following liquid solution: 60 mL Ethanol with 0,050 gr of Chrome(III)oxide (Cr_2O_3) powder. The solution was sonicated for 5 minutes at a level of 9 at a temperature of 24°C.
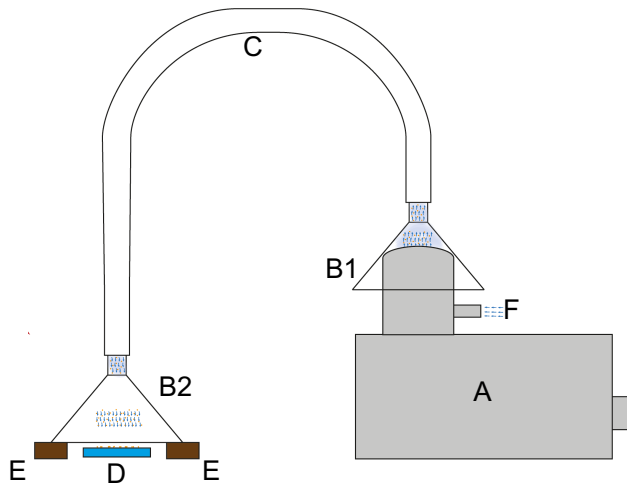
Figure A-5: Represents a schematic overview of the set-up. (a)
Humidifer (Beurer LB12 mini air humidifier), (b) Two cones, (c)
Hosepipe, (d) Glass slide, (e) Small plates and (f) Inlet humidifier,
air pump is mounted on this inlet.

The created vapor from the humidifier (A) is blown away with the air pump into a cone (B1) which was mounted on a hosepipe (C). A smaller cone (B2) was mounted on the other side of the hosepipe. The reason of this smaller cone was to prevent that a lot of vapor would fly past the glass slide (D). The small plates (E) were used to lift the smaller cone a bit so the vapor could fly away and the condensation droplets on the cone (B2) would not drop on the glass slide. Besides this, condensation also occurred on the glass slide
No measurements were taken of the glass slide because of the condensation. Adjustments on the set up were needed to eliminate the condensation problem.

Method 1: experiment 2

This setup, which is represented in Figure A-6, uses the same liquid solution as in experiment 1.
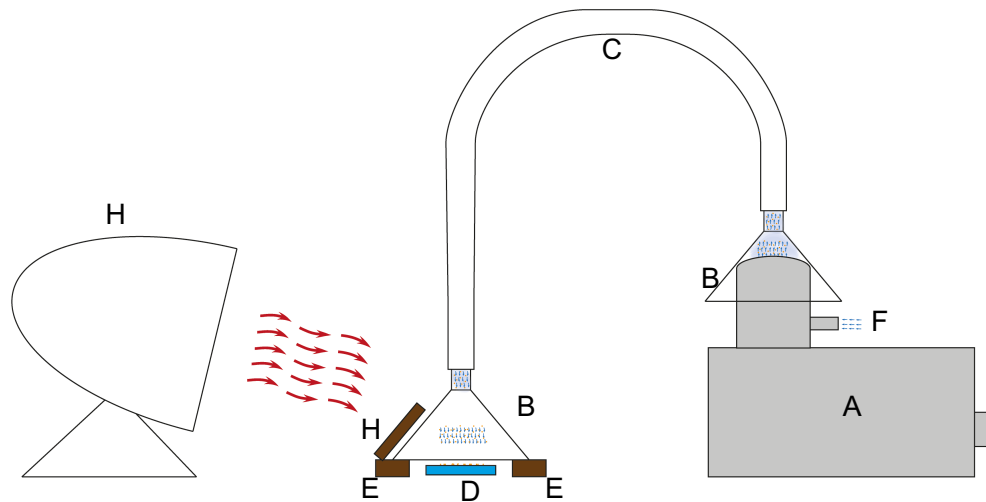
Figure A-6: Represents a schematic overview of the set-up. (a) *Humidifier (Beurer LB12 mini air humidifier), (b) Two cones, (c) Hosepipe, (d) Glass slide, (e) Small plates, (f) Inlet humidifier, air pump is mounted on this inlet, (g) Infrared light and (h) Covering plate.*

The set up and the working principle is the same as in experiment 1. Only in this experiment an infrared light (G) was added to the set up. The infrared light is used to heat up the smaller cone (B) and the glass slide (D). This was done to avoid any condensation of the vapor on the cone or the glass slide.
The temperature of the glass slide was measured under three different conditions:

- Without any heating (Experiment 1)
- With IR light
- With IR light but the glass slide was covered by a metal plate (H)

The temperatures of the glass slide were measured to determine the influence of the IR light, see Figure A-7 for the results. In the three cases the glass slide was placed under the cone till the temperature of the glass slide reached a plateau value before the measurements started.
When no heating was applied the temperature of the glass slide starts with 21.8°C. During the vapor deposition the temperature drops quickly and after 10 minutes it reaches a plateau value of 20.5°C.
When looking at the situation were the IR light was used without covering plate (H), the temperature of the glass slide starts with 53.4°C. When the humidifier is turned on the temperature immediately drops to 48.1°C after 1.5 minute. After this drop, the glass slide warms up again and then it gradually decreases to a value of 43.2°C at 27 minutes. After 27 minutes a small increase of the temperature is visible this comes due to the humidifier which was automatically turned off because of shortage of the liquid solution, no more vapor was created after 27 minutes. With the IR light the glass slide has a temperature between 53.4°C and 43.2°C which can have a negative

influence on the sample which will be mounted on the glass slide. With a high temperature the fiber in this case, can undergo a heat treatment which can dry out the fiber which will have an influence on the hydromechanics of the fiber. It is more favorable to have a temperature which is a bit lower so it will not damage the fiber.

The temperature was reduced by the use of a metal plate to protect the glass slide from any IR light. The glass slide was still heated up because of the environment (small cone and air inside the cone). The glass slide started with a temperature of 38.3°C and decreases gradually to a plateau value of 31°C. The best set up is the set up with the covering plate to reduce the temperature of the slide slide.
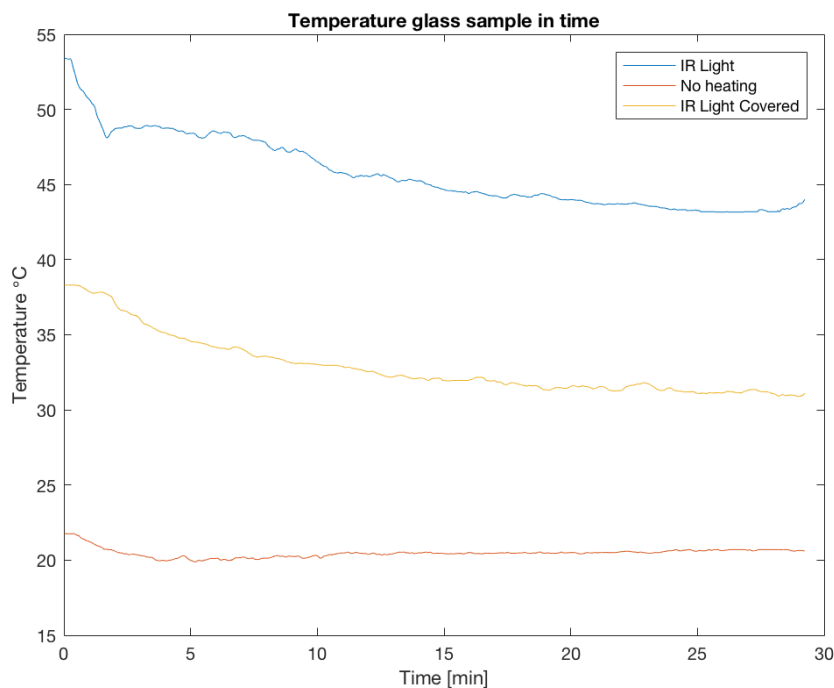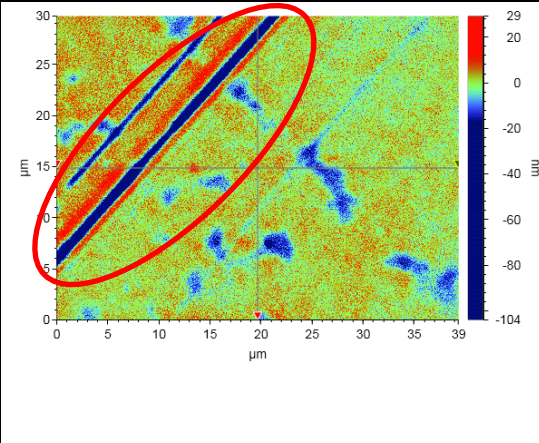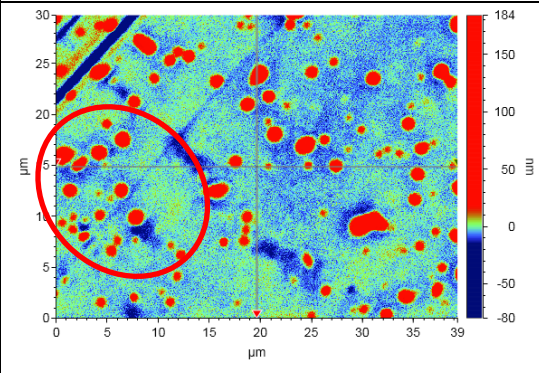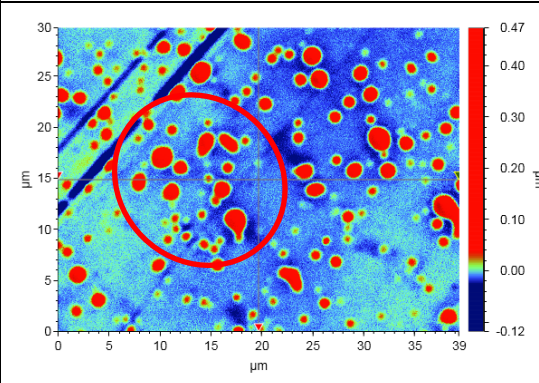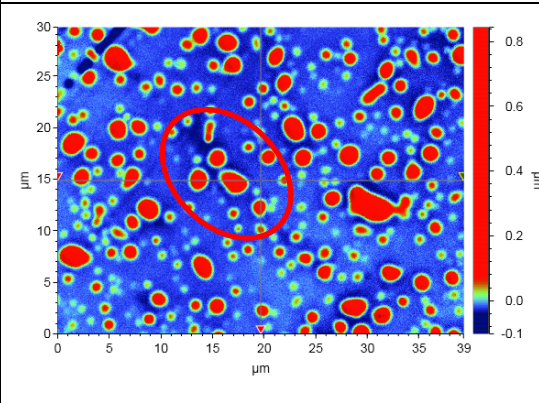
Figure A-7: Temperature graph measured at the glass slide under three different conditions.

The setup of experiment 2, with the covering plate (H), is used during a patterning experiment to gain results of the resulted pattern on the glass slide. The duration of the experiment was 1,5 hours. The images were made with the Bruker with a 100x lens and an internal 2x lens to visualize the pattern. To compare the results in time, images were taken every 10 minutes at almost the same position. In Table A-1 some remarkable images are shown with some short explanations.

Figure A-8: Glass slide on time t=0 min.	The glass slide at time 0. The glass slide is cleaned with the use of a cotton bud, acetone and ethanol. As you can see in the figure there is no dirt on the glass slide. A scratch mark is made on the glass slide to scan every time the same area.
Figure A-9: Glass slide on time t=20 min.	The glass slide after 20 minutes. A homogeneous pattern originates after 20 minutes. The pattern consist out of particles with a size range of 1 to 3 μm. (The marked area is explained in the next figure)
Figure A-10: Glass slide on time t=30 min.	The glass slide after 30 minutes. More particles have landed on the glass slide. Also some clustering starts to happen because particles seem to grow
Figure A-11: Glass slide on time t=60 min.	The glass slide after 60 minutes. (The marked area is explained in the next figure)

Figure A-12: Glass slide on time t=70 min.	The glass slide after 70 minutes. More clustering of particles occur compared with the previous marked area.
Figure A-13: Glass slide on time t=70 min.	The glass slide after 80 minutes. (The marked area is explained in the next figure)
Figure A-14: Glass slide on time t=90 min.	The glass slide after 90 minutes. In this stage of the process more and more particles seem to cluster.

Table A-1: Table of remarkable images, made with the Bruker NPFlex) during patterning by the use of a humidifier (Method 1).

Since the particles became larger in time, we assumed that the particles cluster in time. To verify this assumption, the glass slide was also analyzed under the Scanning Electron Microscope (SEM). Figure A-15 represents the pattern on the glass slide after 1,5 hours. The glass substrate contains particles which are represented by the white grains in the figure. Remarkable is that the Bruker measures more "particles" than actually can be seen with the SEM. The Bruker measures most likely the particles but also the black residue which can be seen in Figure A-15. This conclusion is reliable since the "particles" from the Bruker have round shapes like the residues in the SEM image.
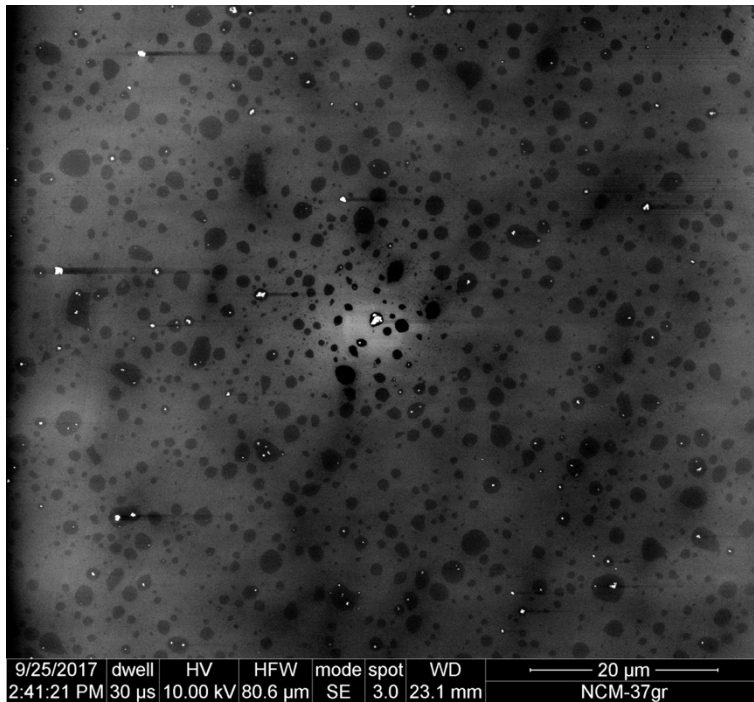
Figure A-15: SEM (Scanning Electron Microscopy) image of a glass slide after patterning with method 1.

A remarkable thing happened when zooming in on one single residue droplet with the SEM. When zooming in on these droplets they disappear in time. This means that it is kind of a wax or liquid which evaporates. Figure A-16 and Figure A-17 show the residue around a particle which disappears in time.
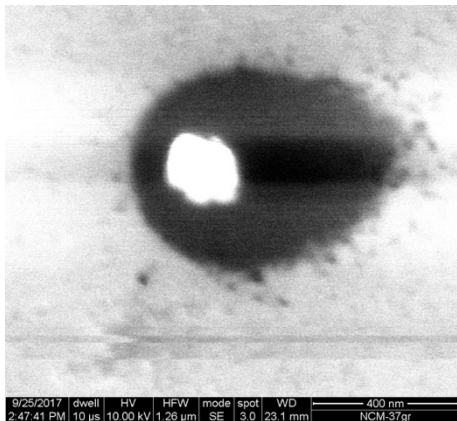
Figure A-16: Zoomed area of a particle surrounded with a residue.
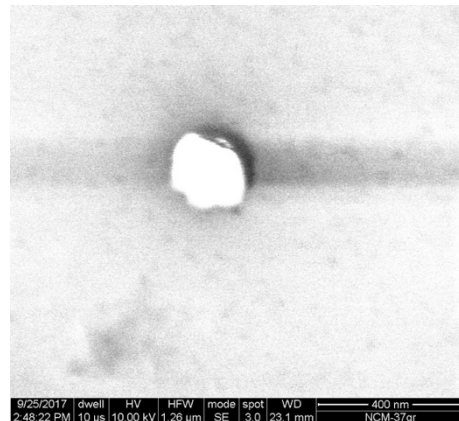
Figure A-17: Zoomed area of a particle after a few minutes of scanning; the residue disappeared.

This residue can come from several things, namely:
- The Chrome(III)oxide (Cr2O3) powder can contain any wax kind of substitute which can come of when it is in contact with ethanol. The reason of this assumption is that every particle on the substrate lays in the middle of a residue droplet.

The Chrome(III)oxide (Cr2O3) powder is heated up to 165°C to see if any wax comes off but this was not the case. Conclusion: the black droplets are probably not from the Chrome(III)oxide (Cr2O3) powder.

- The glue which is used to setup inside the humidifier can be removed with alcohol. Since ethanol is an alcohol it can react with the glue from the glue gun. During the tests the glue came off several times. This is probably due to the reaction with ethanol. Conclusion: the glue from the glue gun reacts with the used ethanol which can create a wax kind of droplets on the glass slide.

- For the setup, old hosepipes are used. Old hosepipes can have an orange colored layer on the inside of the pipes. This orange layer can come off easily with ethanol this might be the source of the residue. Conclusion: Dirt from the inside of the hosepipes can react with the ethanol and can create the strange residue on the glass slide.

To exclude the glue and the hosepipe reaction with ethanol a new setup is built without glue and new unused hosepipes. Chrome(III)oxide (Cr2O3) powder will not be used anymore. Instead a solution of ethanol with microspheres of 1 μm will be used.

Method 1: experiment 3

This setup, which is represented in Figure A-18, uses the following liquid solution: 60 mL Ethanol with 500μL of silica particles with a size of 1 μm. The solution was sonicated for 5 minutes at a level of 9 at a temperature of 24°C
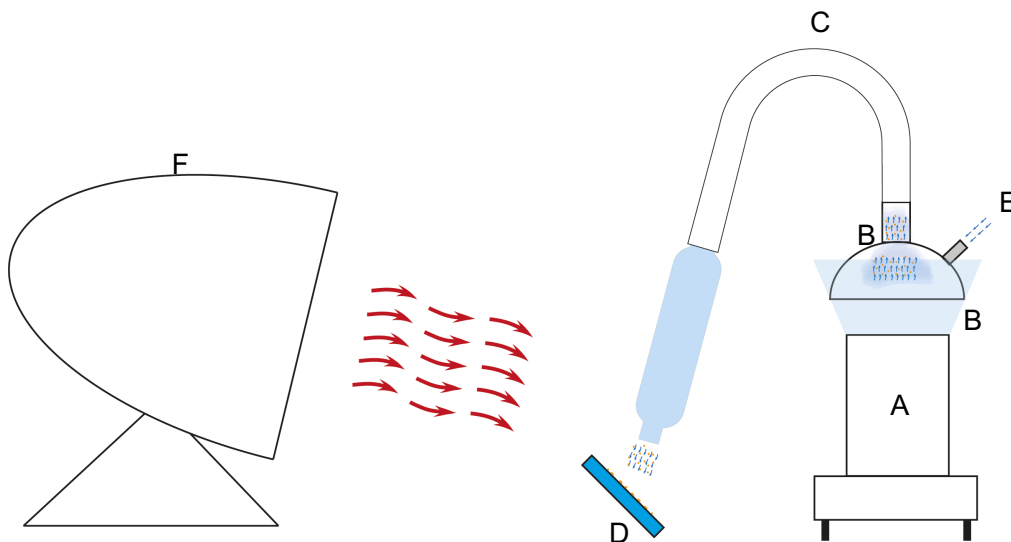
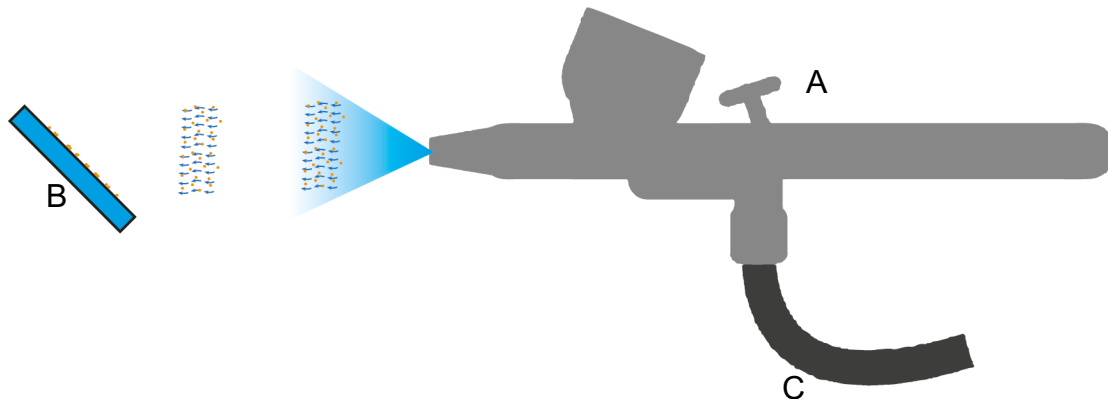*Figure A-18:* Represents a schematic overview of the set-up. (a) *Humidifier housing, (b) Two cones, (c) Hosepipe, (d) Glass slide, (e) Inlet humidifier, air pump is mounted on this inlet and (f) Infrared light.*

The setup and the working principle is the same as in experiment 2. In this case the electronics are taken out of the Beurer LB12 humidifier and mounted on a manufactured humidifier housing (A). This setup is made without glue since it gave us problems in experiment 2. The thickening on the end of the hosepipe (C) reduces the velocity of the vapor. The infrared light (F) has more

time to heat up the vapor in the thickening before it lands on the glass slide. Since the glass slide is not heated up directly and the setup does not use a cone over the glass slide, as was done in experiment 2, no covering plates are needed because the vapor does not cause any condensation on the glass slide anymore.

The setup is tested and is able of creating patterns on a glass slide with different sizes of particles. The maximum size of the particles can be calculated by the equation which was given by Lang [16]:

$$D = 0.34 \left(\frac{8\pi T}{\rho f^2}\right)^{\frac{1}{3}} \qquad\qquad (\ A.1\ )$$

$D = droplet\ size\ [\mu m]$
$T = surface\ tension\ [mNm^{-1}]$
$\rho = liquid\ density\ [kg/m^3]$
$f = frequency\ [Hz]$

In the case of an ethanol based solution droplet sizes of 2.1 μm will be generated by the humidifier. Conclusion: the working patterning method can generate patterns with a maximum particle size of 2 μm. Particles of 1 μm and 500 nm size are tested on a glass slide, results are shown in the next chapter.

Method 2: experiment 1
This setup, which is represented in Figure A-19, uses the following liquid solution: 5 mL Ethanol with 50μL of silica particles with a size of 1 μm. The solution was sonicated for 5 minutes at a level of 9 at a temperature of 24°C

Figure A-19: Represents a schematic overview of the set-up. (a) *Airbrush gun, (b) Glass slide and (c) Inlet airbrush gun, air pump is mounted on this inlet.*

The airbrush gun is used with an air pressure between 1~2 bar. The higher the pressure the smaller the droplets. A disadvantage of a higher pressure is the airflow which becomes higher as well. This higher airflow can damage the sample. Conclusion: The set up works and is capable of creating a good particle pattern. In the experiments a pressure of 1 bar is used and the results are shown in the next chapter.

Results of the patterning methods

For both methods the patterning is a time related process. Clustering of the particles on the glass slide increases when the time of patterning increases. The best pattern is obtained just before clustering occurs. This patterning time and clustering depend on several things namely:

- Distance between patterning method outlet and glass slide.
  Changing the distance between the patterning method outlet and the glass slide will change the time of spraying due to the amount of particles which will land on the glass slide. The larger the distance the more particles will fly past the glass slide and vice versa.

- Solution ratio
  Changing the solutions ratio will change the amount of particles in a solution. The larger the ratio the more particles will and can land on the glass slide.

- Particle size.
  Changing the particle size will change the time of clustering. Larger particles will cluster earlier and more. For example, Figure A-20 and Figure A-21 representing a pattern made with 3 µm and 500 nm particles. Both images were taken with an optical microscope with a 50x lens. The images were made after 4 minutes of patterning with an airbrush gun. The pattern with the 3 µm particles has a lot of clustering and is not that dense comparing with the pattern made with the 500 nm particles. Since 3 µm particles cluster too much, no dense results could be obtained so for further experiments, only particles sizes of 1 µm and 500 nm will be used.
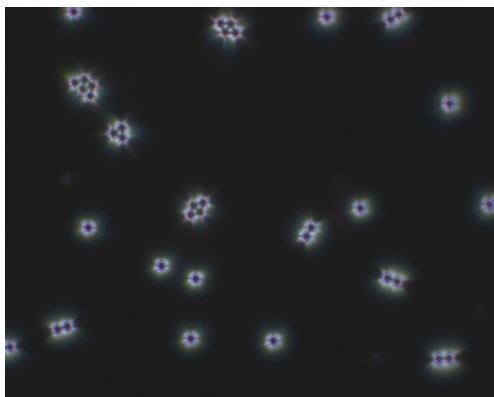
Figure A-20: Particle pattern of 3 µm created with the airbrush. Image were obtained with an optical microscope with an 50x lens. Field of view: 273.9 x 216.4 µm.
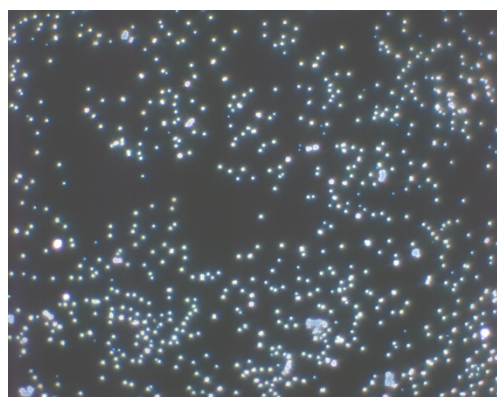
Figure A-21: Particle pattern of 500 nm created with the airbrush. Image were obtained with an optical microscope with an 50x lens. Field of view: 137.8 x 108.7 µm.

Figure A-22 - Figure A-25 represent the best obtained patterns for 1 μm particles used for both patterning methods. The density of the patterns for both techniques are comparable. Some clustering happened in both cases but it is still acceptable. A remarkable difference in the both techniques is the time. With the humidifier it takes approximately 4x longer to create the same dense pattern compared to the airbrush gun.
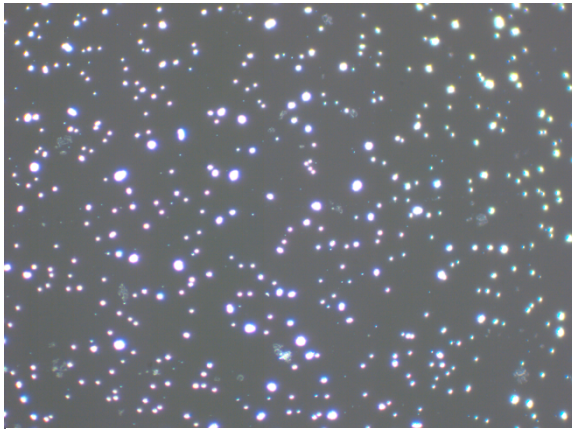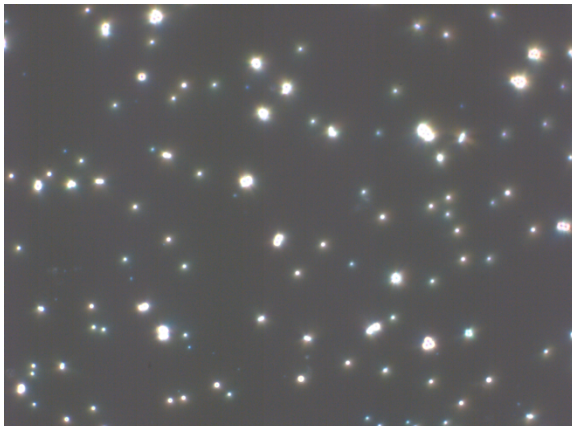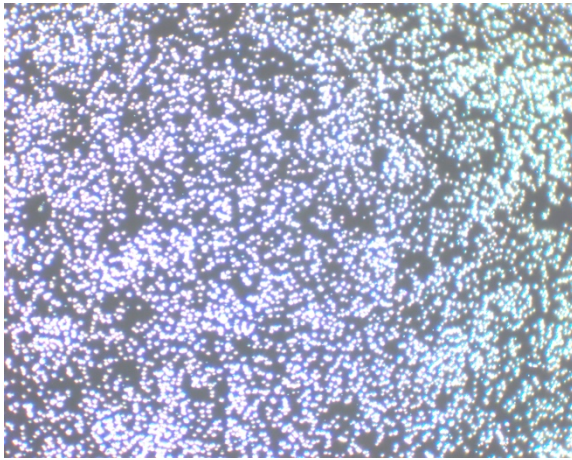

Figure A-22: Pattern on a glass slide with particles of 1 μm after 12 minutes made with the humidifier. Image were obtained with an optical microscope with an 50x lens. Field of view: 273.9 x 216.4 μm.
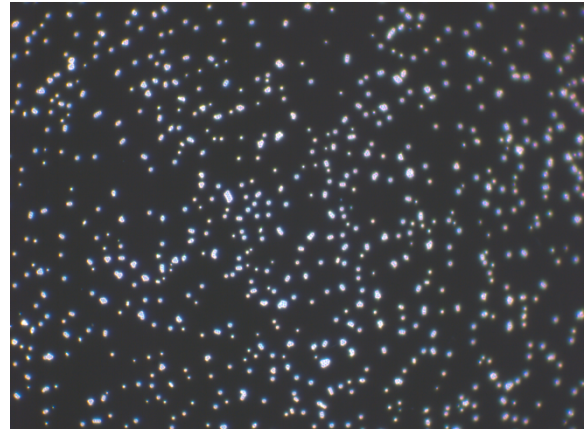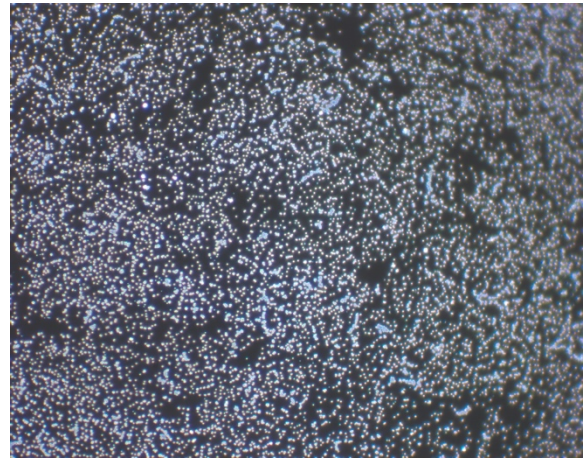

Figure A-23: Pattern on a glass slide with particles of 1 μm after 3 minutes made with the airbrush. Image were obtained with an optical microscope with an 50x lens. Field of view: 273.9 x 216.4 μm.
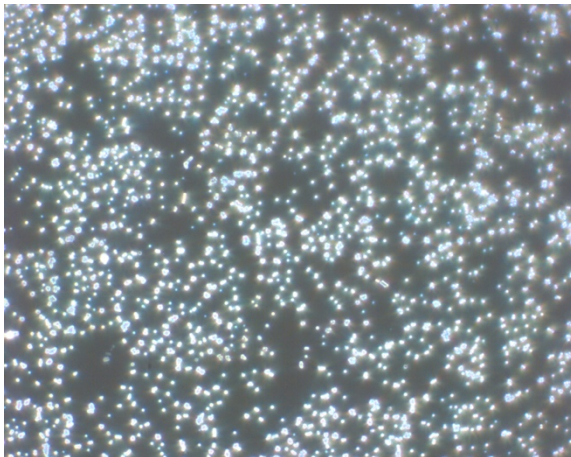

Figure A-24: Pattern on a glass slide with particles of 1 μm after 12 minutes made with the humidifier. Image were obtained with an optical microscope with an 100x lens. Field of view: 137.8 x 108.7 μm.
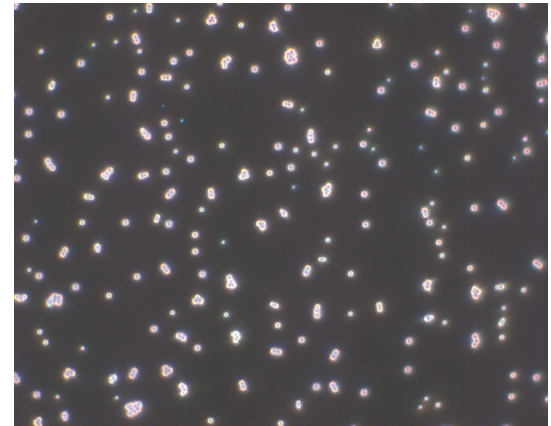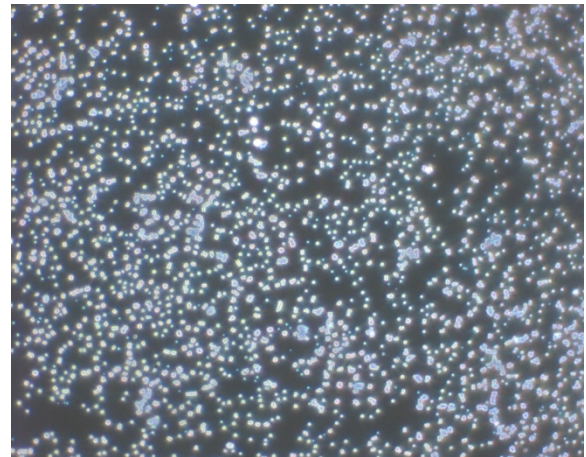

Figure A-25: Pattern on a glass slide with particles of 1 μm after 3 minutes made with the airbrush. Image were obtained with an optical microscope with an 100x lens. Field of view: 137.8 x 108.7 μm.

Conclusion

From the results we can conclude that both patterning methods can obtain the same patterns. A big advantage of the humidifier is the lower airflow which is used. With the airbrush gun higher airflows are needed which can damage a fragile sample. The big advantage of the airbrush gun is the low amount of particle solution which is needed. The airbrush uses 4x less amount of particle solution compared to the humidifier. Besides the usage of the particle solution also the time is a small advantage. The airbrush for example can create 500 nm patterns in 7 minutes were the humidifier needs at least 12 minutes.
The densest pattern can be obtained with 500 nm particles since it clusters less, this is an advantage for GDHC since the 500 nm particles can be sprayed homogenous over the whole fiber surface. However, the 1 μm particles do have a larger topography gradients than 500 nm particles, which can be also an advantage during GDHC. For further experiments the airbrush will be used since it is easier to use and it uses less particle solution.

Appendix B: Comparison of the profilometers

As mentioned earlier profilometry will be used for obtaining detailed topologies of the fiber surfaces. During the optimization of the profilometry the focus was on the Bruker NPFlex and the Sensofar PLµ 2300.
The difference between these two profilometers is the working principle. The Bruker NPFlex works with vertical scanning interferometry (VSI). With this technique light from the source is divided into two beams by a beam splitter and recombines them to create an interference pattern. The interference pattern is then used to determine the difference in path length which is used to determine the height of the sample.
The Sensofar PLµ 2300 on the other hand works with optical confocal profilometry. With this technique the sample is scanned vertically in steps so every point on the sample passes through the focus. The height of the sample surface at each pixel is then calculated once a bright spot is observed.
The most suitable profilometer is determined by the use of simple GDHC experiments.

Experimental method for comparison profilometer

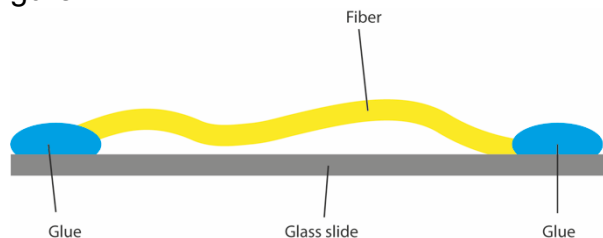For this experiment a toilet paper fiber is used and glued on both ends on a glass slide, see Figure B-1.

Figure B-1: Schematic view of a fiber glued on a glass slide.

This single fiber is used for both profilometers to have an identical sample in both cases. In both cases the profilometer was configured with different settings. For every setting configuration 12 images were obtained of the sample. 6 Images were made with a rigid body motion in the X-axis and 6 images were made with a rigid body motion in the Y-axis. These rigid body motions were created by moving the stage approximately 10 µm in X- or Y-direction. Starting from position 0 and every image was taken 10 µm further away from the starting position which results that image 6 was taken at a position 60 µm moved from the starting position.

These obtained images were used for Global Digital Height Correlations (GDHC). In both directions (X-axis and Y-axis) 6 correlations were done with the obtained images. Every correlation gives a residual field as outcome. The residual fields contained some NaN filled pixels, due to the masking feature which was used in the GDHC correlations, see Appendix C: for explanation of

this feature. For every setting configuration of the profilometers, 12 (6 in the X direction and 6 in the Y direction) correlation values were obtained by averaging the residual fields to quantify a correlation. In every direction the mean of the 6 correlation values was taken to create two different average correlation values, one in each direction. From these two average correlation values the mean was taken to create an overall correlation value which quantifies the used setting of the specific profilometer. Finally, all the setting configurations on the profilometers are factorized with an overall correlation value which gives an insight in the quality of the GDHC correlation. See Figure B-2 for a schematic overview of the factorizing of every single setting of a profilometer mentioned above. With the above described method the most suitable profilometer will be determined. This conclusion is not binding but it gives an insight in the settings and the profilometers when working with fibers.
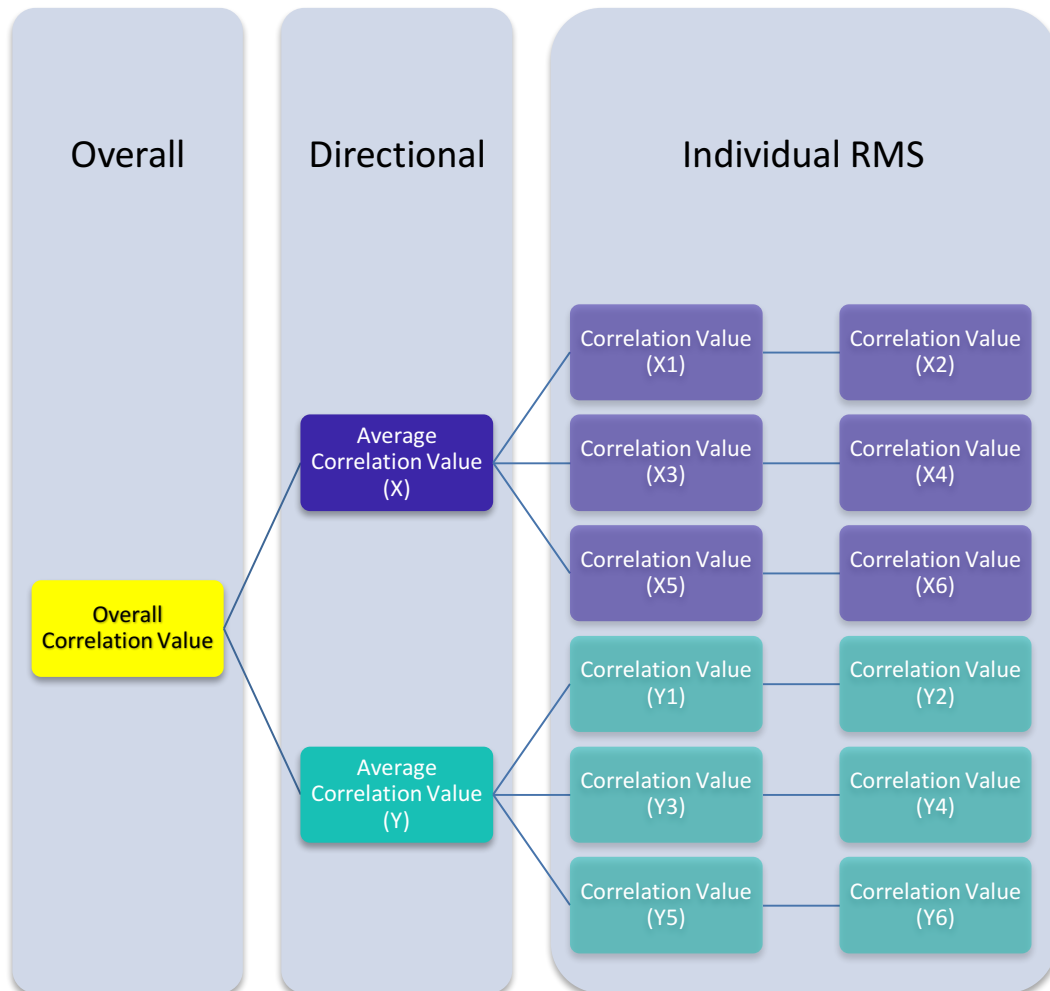

Figure B-2: Overview of factorizing a specific setting for one profilometer with the different correlation values, average correlation values and the final overall correlation value.

Experimental methodology and results for comparison profilometer

Sensofar PLμ 2300

The Sensofar has 2 different settings that can be changed for topologies namely, the threshold and the intensity of the light source. The threshold determines the minimum reflected light intensity, intensity of the light which is reflected from the fiber surface, which is used for constructing topologies. Pixels with reflected light intensities lower than the threshold will not be used for creating topologies. Smooth surfaces produce high contrast fringes so the threshold is normally set high (for instance, 15%). Rough surfaces, or surfaces with high angles or low fringe contrast normally needs a lower threshold. This will allow lower light intensities to pass the threshold, a disadvantage of a low threshold is increased system noise. Figure B-3 shows a light intensity vs surface height plot for a single pixel in the image. A smooth surface with a height step will result in a steep parabolic graph (purple) since with smooth surfaces there is less noise. The surface height of that specific pixel is found by finding the highest reflected light intensity. A high threshold can be used because of the steep parabolic shape of the figure. A lower threshold in this case will eventually result in more noise since more reflected light and scattered light will be used for creating a topology.
When looking at the rough surface it is different. When lowering the threshold more reflected light is used to determine the height of a single pixel which makes it easier in this case to find the maximum light intensity. However, when the threshold is chosen too low more noise will be added to the results.
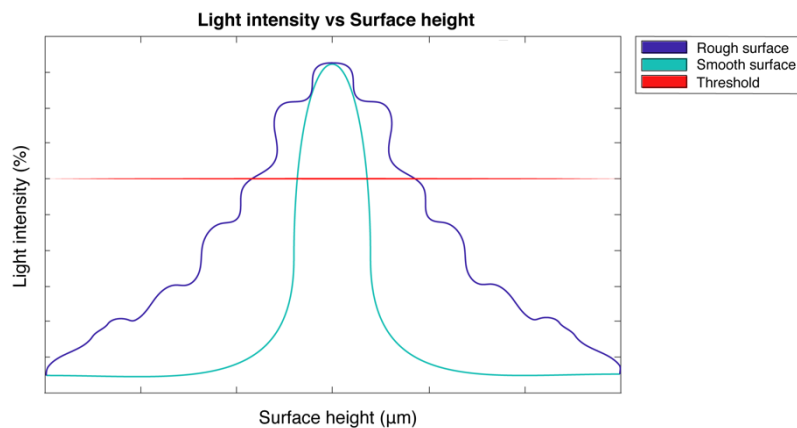

Figure B-3: Graph of light intensity vs surface height for a smooth and rough surface for a single pixel in the image.

The intensity of the light source is in other words the amount of photons which are exposed on the sample. The light intensity is based on a range of 0-100% and is comparable with a dimmer. Increasing the intensity will increase the amount of photons. This will increase also the amount of photons that can be detected so more information of your sample will be detected. A disadvantage of a maximum light intensity is overexposure. At a certain time, the sample is

overexposed due to the intensity and the software cannot calculate the height of your sample so it will return zero information over the exposed area.
For the Sensofar the threshold is set automatically at 10%, the light intensity is calculated at 18% by the software itself. Lower intensities will automatically reduce the amount of information in the resulted topology image. These settings are used to create a set of different settings to cover the whole setting range that are useful in the case of a fiber. See Table B-1 for the settings that are used during the experiments.

Light source		
Magnification	Threshold	Light source intensity
50x	10	18
50x	10	28
50x	10	38
50x	10	48
50x	10	58
Threshold		
Magnification	Threshold	Light source intensity
50x	1	18
50x	2	18
50x	3	18
50x	4	18
50x	7	18
50x	10	18
50x	13	18
50x	16	18
50x	19	18

Table B-1: All the different used settings for the Sensofar

For every setting 12 measurements are done as described in previous chapter. The obtained topologies are further used in GDHC correlations. The settings for the GDHC are set very basic because only a rigid body motion is applied on the fiber. See Table B-2 for the settings for the GDHC correlations.

Option	
Coarse grain steps	0
Conversion criteria	1e-4
Maximum iterations	100
Basis shape function	Polynomial
Order shape function	0
Gradient	F
Dilation mask*	1

Table B-2: Used settings for the GDHC correlations.

* This setting is explained in Appendix C

Change in light intensity

A strongly increase of the average correlation value occurs for an increased light intensity, see Figure B-4**.** When increasing the light intensity more topology information about the fiber surface becomes visible. The reason of the high average correlation value for the light intensity of 48 and 58 is the overexposure effect. At the edges of these overexposed areas the correlation values will be very high so these edges of the overexposed areas have a high influence on the average correlation value.

For the light intensity of 18%, 28% and 38% there is no overexposure but there is still an increase in the average correlation value. Since we are only interested in the setting which results in the lowest average correlation value a light intensity of 18% is chosen. With a light intensity of 18% robust surface images can be made which lead to the lowest average correlation value.
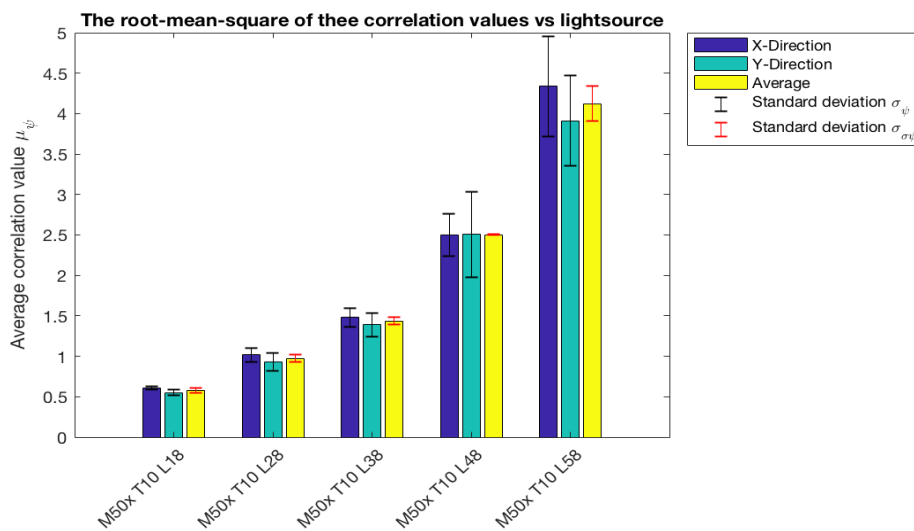

Figure B-4: Average correlation value for different intensities of the light source for the Sensofar

Change in threshold

An increased threshold leads to a strongly increasing trend of the average correlation value, see Figure B-5(a). When lowering the threshold, the amount of system noise will increase as explained earlier. This is visible when looking at the average correlation value for a threshold of 1%. With a threshold of 1% height information arises on the outside of the fiber area itself. This means that the threshold is set so low that even scattered light is being detected and used for creating the topology, which will lead to a high average correlation value. This is also visible when looking at the amount of visible pixels (Figure B-5(b)), with a threshold of 1% the amount of pixels is almost 1,5 times higher than with a threshold of 2%.

For the thresholds of 2, 3 and 4 scattered light is not detected anymore because all the information that is being detected is near the actual area of the fiber. A fiber has round stepwise edges which are very difficult to detect when using profilometry because of their steepness. These edges are sensitive for noise which lead to high average correlation values. Because of the low thresholds (2, 3 and 4) these noisy edges of the fiber surface are also used for creating the topology of the images.

When increasing the threshold from 4% to 10% a decrease of the average correlation value occurs. From threshold 10% upwards to threshold 19% the average correlation value reaches a plateau value while the amount of pixels is still decreasing. In conclusion, thresholds lower than 4% will lead to unstable correlations with high average correlation values. A threshold of 10% is the best solution since it has one of the lowest average correlation values but it has the most amount of pixels compared to other thresholds with approximately the same correlation value. More filled pixels will eventually lead to more detailed strain fields in the later GDHC.
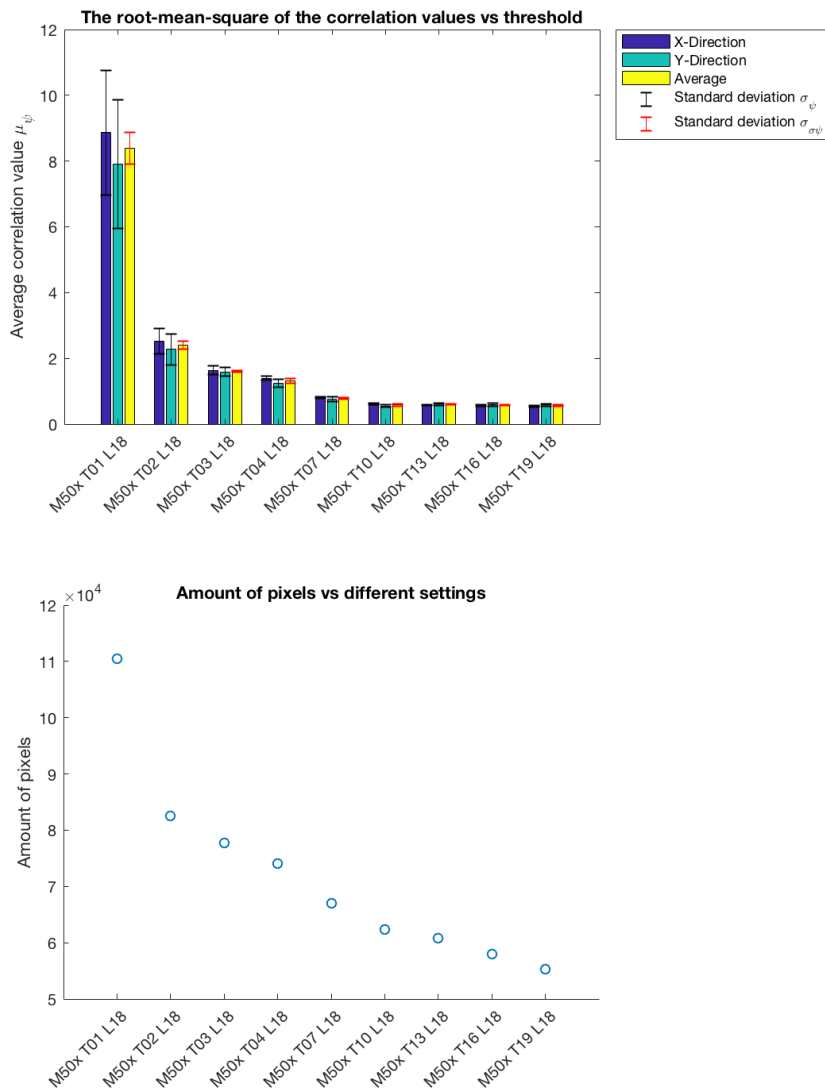

Figure B-5: (a) Average correlation value for different threshold settings (b) Amount of visible pixels in the obtained images for every used threshold setting for the Sensofar.

Bruker NPFlex

The Bruker has 3 different main settings that can be changed namely, the threshold, the light intensity and the type of the light source. The light intensity and the threshold settings work the same as for the Sensofar. The Bruker works with white or green light as a light source.

The Bruker is automatically set at a threshold of 5% and a light intensity for white light is calculated at 20% and for green light it is calculated at 8%. Also this is calculated automatically by the software.

These settings are used to create a set of different settings to cover the whole setting range that are suitable for the fiber. See Table B-3: for the settings that are used during the experiments.

Light source			
Magnification	Threshold	Light	Light source intensity
50x	5	Green	5
50x	5	Green	6
50x	5	Green	7
50x	5	Green	8
50x	5	White	18
50x	5	White	20
50x	5	White	22
50x	5	White	24
Threshold			
Magnification	Threshold	Light	Light source intensity
50x	1	Green	8
50x	2	Green	8
50x	3	Green	8
50x	4	Green	8
50x	5	Green	8
50x	1	White	20
50x	2	White	20
50x	3	White	20
50x	3	White	20
50x	5	White	20

Table B-3: All the different used settings for the Bruker.

For every setting 12 measurements are done as described in previous section. The obtained topologies are further used in GDHC correlations. The settings for the GDHC are the same as for the experiments with the Sensofar, see Table B-2 for the settings for the GDHC correlations.

Change in light intensity
When looking at the influence of the light intensity on the average correlation value it is possible to recognize two different mean heights of the bar plots, see Figure B-6(a). The average correlation values of the green light source are lower than the average correlation values while using a white light source.

This can be explained due to the fact that white light uses the waves length of the whole light spectrum to measure the height of a sample while the green light only uses the green light wave lengths to measure the height of a sample. This means that the green light source works with a narrower bandwidth which makes it more precise in interferometry.

In both cases (green and white light) the average correlation values due to the light intensity settings do not vary that much. On the other hand, the amount of visible pixels does vary a lot, see Figure B-6(b). The focus for the light intensity setting will only be on the green light source since it results in a lower average correlation value than the white light source and the amount of visible pixels is much higher. When looking at the light intensities 6%, 7% and 8% these average correlation values alter a small bit so this means that there are minor differences between these settings. When increasing the light intensity from 6% to 8% the amount of pixels increases but the correlation value stays almost the same. This is probably due to the robustness of the extra gained visible pixels.

When looking at the average correlation value and the amount of pixels, the setting with the light intensity of 8% has the lowest average correlation value but also the most amount of visible pixels. This is also the automatically determined light intensity from the software.
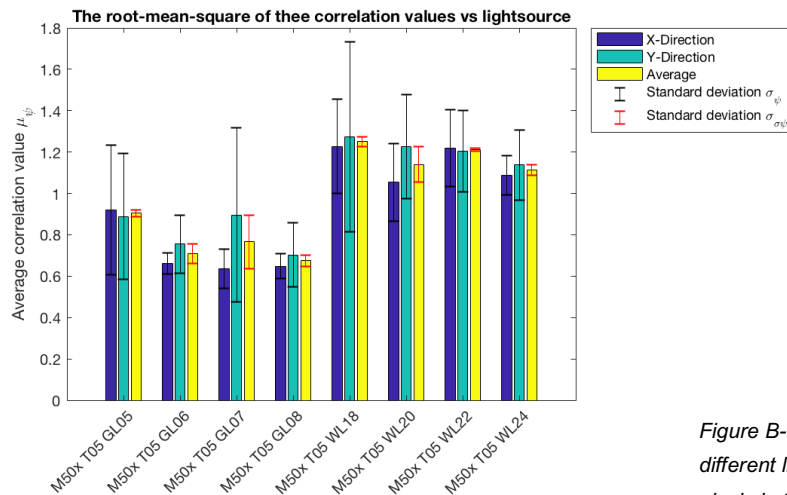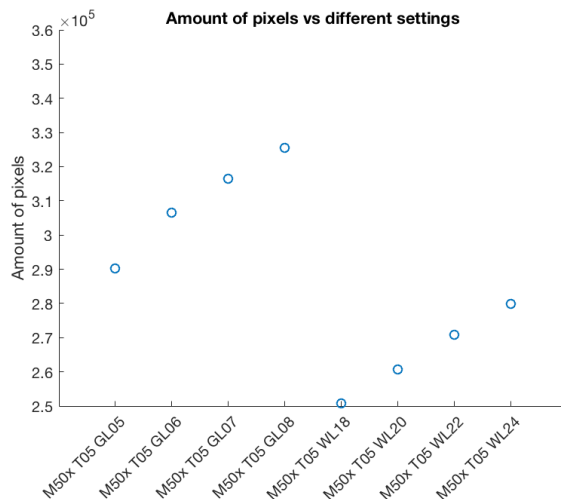

Figure B-6: (a) Average correlation value for different light source settings (b) Amount of visible pixels in the obtained images for every used light source setting for the Bruker.

<u>Change in threshold</u>

In the case of the threshold the same kind of trend happened as when looking at the light intensity setting, see Figure B-7 for the results. The green light source settings have a lower average correlation value than the white light source settings, the reason is explained earlier.

When looking at the white light source a conclusion can be drawn, that the average correlation value is not really influenced by the threshold since the average correlation values of all the white light settings lie in the same range. The threshold of green light settings instead does have an influence on the average correlation value. Also in this case the focus for the threshold setting will only be on the green light source since it results in a lower average correlation value than the white light source and it results in much higher amount of visible pixels, see Figure B-7(b) . When looking at the green light settings it is possible to see that the average correlation value and the amount of pixels decreases when the threshold is increasing. This means that the amount of pixels, with relatively high correlation errors is decreasing while the threshold is increasing. Remarkable is the fact that the average correlation value slightly increases when the threshold is changed from 4 to 5. This increase is so small that the average correlation values still lie in the same range. The small increase can be explained by the correlations that are done in the Y-direction with a threshold of 5. The deviation is larger than the deviation in the Y-direction with a threshold of 4. This larger deviation may be due to a few poor correlations which result in a relatively higher correlation value in the Y-direction. A threshold of 4 results in the best solution since it has one of the lowest correlation values but it has the most amount of filled pixels.
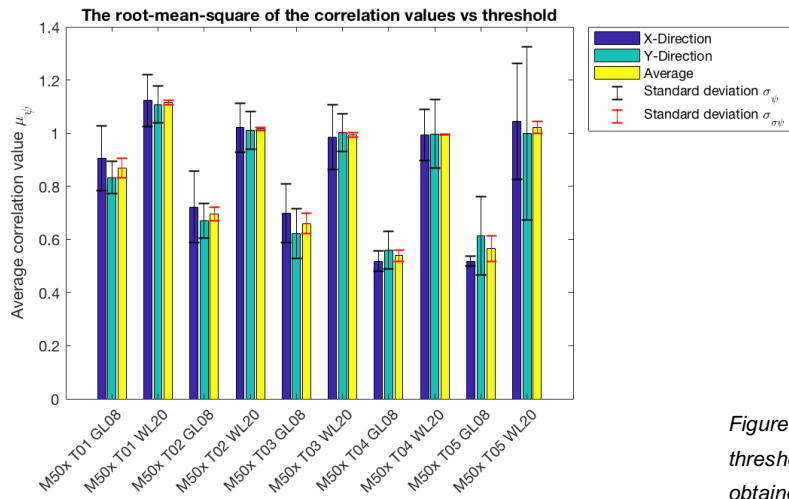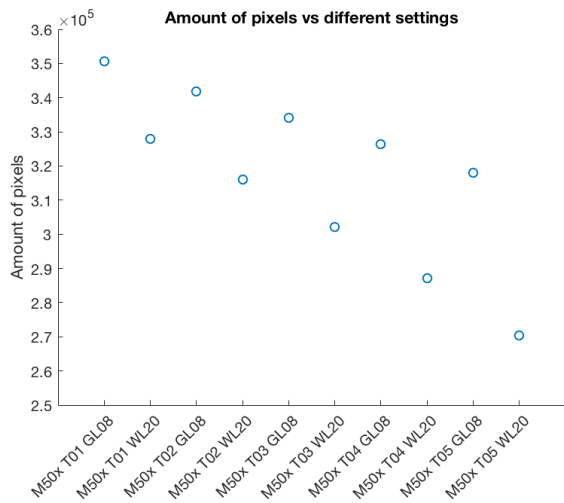
Figure B-7: (a) Average correlation value for different threshold settings (b) Amount of visible pixels in the obtained images for every used threshold setting for the Bruker.

Conclusion of comparison profilometer

To compare the Sensofar with the Bruker only the best results for each of the profilometers are used. The best settings for the Sensofar and the Bruker are shown in the table below. Worth nothing, these best settings are fiber and magnification related, other fibers can have different best settings.

	Sensofar	Bruker
Magnification	50x	50x
Field of view (μm)	254.64 × 190.9	175.7 × 132.8
Size images (pixels)	768 × 576	1376 × 1040
Light source intensity	18%	8% (Green Light)
Threshold	10%	4%

Table B-4: Best settings for both profilometers (the Sensofar and the Bruker).

When looking at the average correlation values it seems that for both profilometers the outcome is almost the same, see Figure B-8. The overall correlation values lie in the same range so we can conclude that both profilometers will give us almost the same results from GDHC by the use of topologies images of the fiber surface. The amount of filled pixels gives a remarkable difference since the Bruker NPFlex created images of the sample with 5 times more filled pixels then the Sensofar PLμ 2300. Figure B-9 represents the images of the sample made with the Bruker and the Sensofar. This leads to a preference for the Bruker since the strains of a fiber can be calculated more precisely with a higher amount of filled pixels (more information about the fiber surface is gained). Another practical advance of the Bruker is the extra 2x magnification lens that can be used inside the machine. This creates a 2x50 magnification with the working distance of a 50x magnification lens. This can be practical because of the space limitations in the climate box which will be used further in the project.
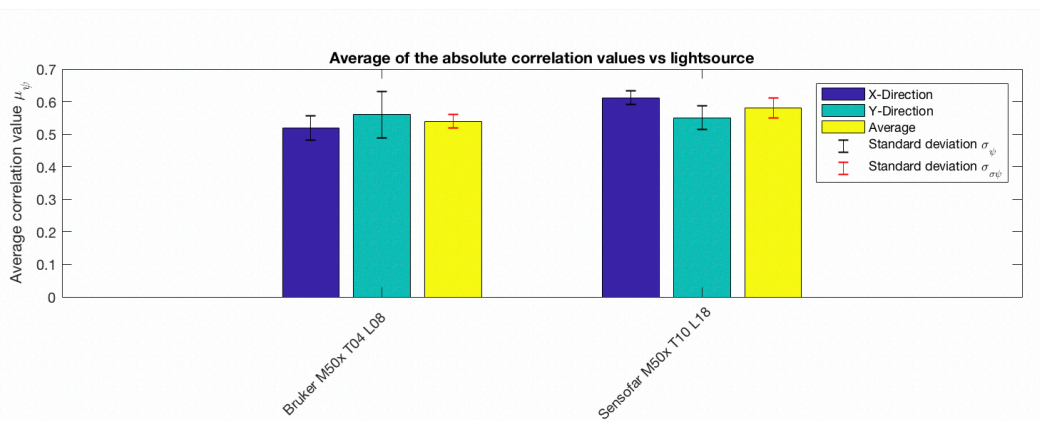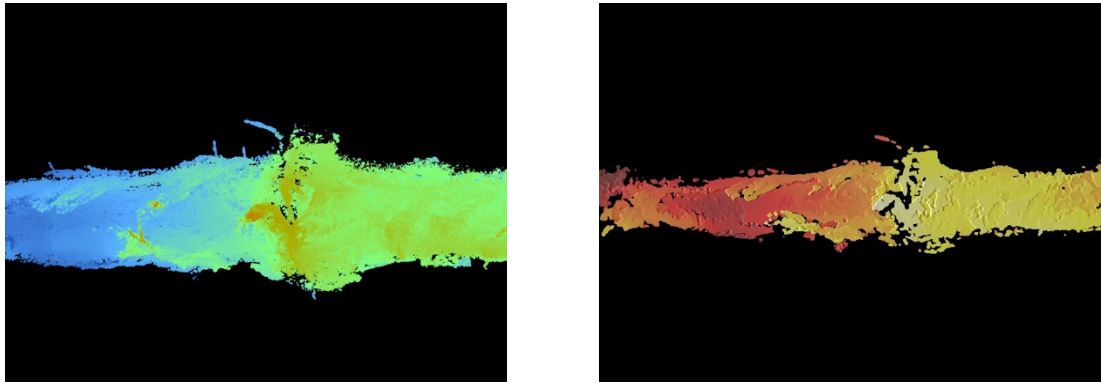

Figure B-8: Average correlation values for the best settings of the Sensofar and the Bruker.

Figure B-9: : (a) Topology image obtained with the best settings of the Bruker. (b) Topology image obtained with the best settings of the Sensofar

Appendix C: Global Digital Height Correlation settings

In this appendix the settings for the GDHC are determined and optimized by doing a relative humidity experiment. During the experiment a single paper fiber was exposed to a changed relative humidity. The relative humidity was changed from 50% to 80% at a rate of 10% RH/hour. The temperature was kept at 23 °C.

Initial GDHC settings

Coarse grain step:
As described earlier, coarse graining is a method which creates images by averaging a group of 2 x 2 pixels into super-pixels. This operation can be repeated on the super pixeled images to create even coarser images, so-called coarse grain steps. Coarse graining is set to 0 (no coarse graining), since fibers have a relative flat surface with low gradients. The samples are prepared with nano particles to create some random gradients on the fiber surface so by coarse graining the advantage of the pattern will be decreased.

Convergence criterion:
As described earlier, the convergence criterion is a criterion which determines if the iterative system is solved. The chosen criterion is such that the norm of the DOF increments, $\underline{\delta\lambda}$, becomes sufficiently small . The convergence criteria is at $\|\underline{\delta\lambda}\|<10^{-4}$.

Maximum iterations:
The maximum iterations is set to 500, which allows the iterative system to iterate till a maximum of 500 iterations is reached.

Basis shape function:
As described earlier, the shape functions can be thought as a function that describe the form (shape) that a displacement field may take. These shape functions can have different basis, i.e. polynomial basis. The polynomial basis shape function was chosen to describe the displacement field. Firstly, because they can describe the mostly global problem physics. Secondly, Bastawrous [8] used the same basis shape function so for making a comparison we chose the same basis shape function.

Order shape function:
As described earlier, the order of the shape function determines the amount of degrees of freedom. The choice of the order of the shape function and its basis determine the kinematic freedom of the solution space. From the results of Bastawrous [8] a conclusion was made that the 4th order of the polynomial

basis shape function would be sufficient. With this in mind the order of the shape function was chosen to be 4.

Masking:

As described earlier, the masking function masks specific pixels from the calculations. Masking is used since the obtained topologies of the fiber surface contains pixels with zero height information and these pixels are labeled with a NaN value and cannot be used during GDHC correlations. Figure C-1 represents the topology of a fiber surface, the black colored areas are the pixels without any height information so they are filled in with a NaN value. A specific masked pixel in the reference image will not always be the same pixel as in the backdeformed image. To tackle this problem a dilation of the masked pixels is used. The dilation is done by masking the surrounded pixels around a masked single pixel by an x amount of rows. Figure C-1 represents the topology images with a dilatation of 1, 2 and 4. In this case the dilation is set to 1 amount of rows around a single masked pixel.
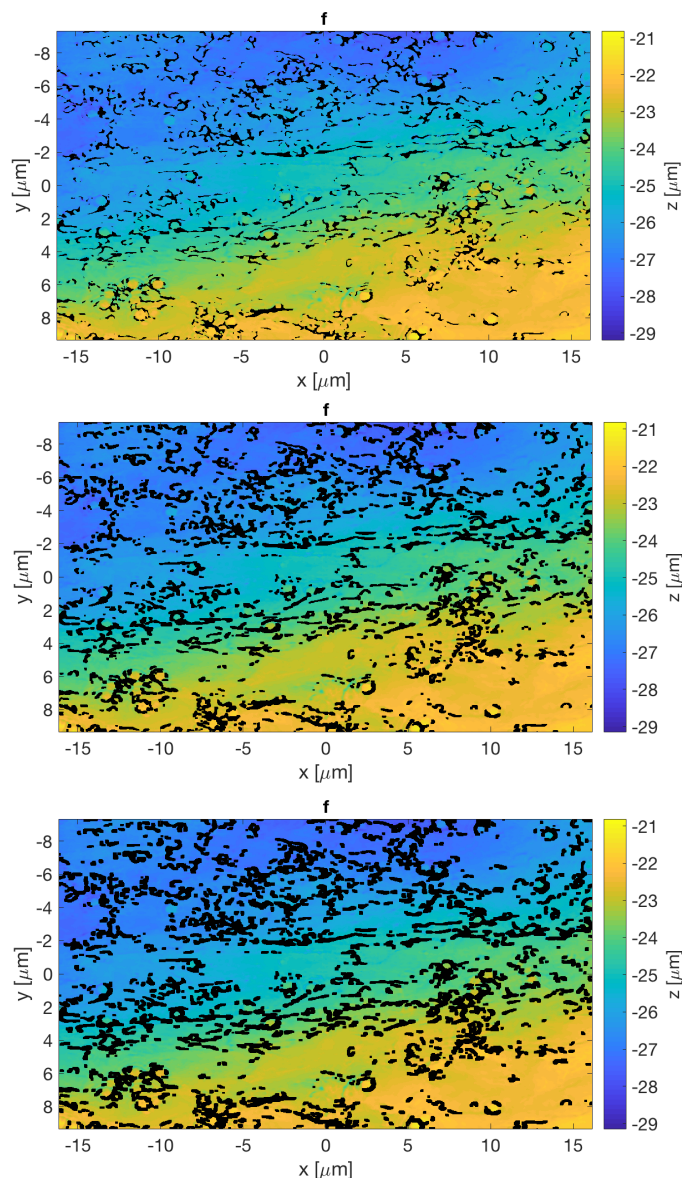

Figure C-1: (a) Reference image f with NaN filled pixels (black pixels), (b) Reference image f with a dilatation of NaN filled pixels of 2 and (c) Reference image f with a dilatation of NaN filled pixels of 4.

Reconstructed height data:
Besides NaN filled pixels in the reference image also the deformed image contains NaN filled pixels. The masking function deletes all the dilated NaN filled pixels in the reference image but it can be that some NaN filled pixels in the deformed image are not included in this mask. To tackle that problem, all the NaN filled pixels in the deformed image are replaced by reconstructed height data. This reconstructed height data is obtained by taking the mean height of the fiber surface in de deformed image.

Gradient:
As described earlier, the gradient function determines the gradient of the image with respect to the spatial coordinates. In this experiment gradient f is chosen since it takes the gradient of the reference image and not from de deformed image. Taking the gradient of the deformed image will introduce noise since the NaN filled pixels are replaced with reconstructed data.

Initial results of a relative humidity experiment

During the experiment a single paper fiber was exposed to a changed relative humidity. The relative humidity was changed from 50% to 80% with a rate of 10% RH/hour. The temperature was kept at 23 °C.
343 Topologies of the fiber surface were made with the Bruker with a green light source with a light intensity of 23%, a threshold of 2% and a 100x magnification lens. These settings differ from de best settings in Appendix B, as mentioned earlier, the settings are fiber and magnification related. The light intensity in this case is automatically determined by the software. The threshold is chosen low, so a lot of fiber information is used for obtaining the topology images. A 100x lens is used since it creates more detailed topologies of pattern on the fiber surface. Figure C-2 represent the outcome of the final correlation between the first and last images of the experiment.
The right images represent the outcome gained with a 4th order polynomial shape function as was proposed by Bastawrous [8]. The residual field (Figure C-2d) shows already a lot of areas with high residuals which indicates that the GDHC correlations did not converge properly. The longitudinal strain ε_{ll} (Figure C-2e) has large fluctuations of compression and extension strain areas over the fiber surface which indicate that the GDHC correlation is unreliable since we would expect a more global extension or compression strain field with some small fluctuations. Looking at the transverse strain ε_{tt} (Figure C-2f), these large fluctuations do not occur which means that the strains in transverse direction are more reliable. Overall the results are unreliable and not accurate. The reason for this can be that the 4th order polynomial is not sufficient enough to capture the whole kinematics of the fiber surface during the experiment.
Even with the 8th order polynomial shape function the residual field (Figure C-2a) shows a lot of areas with high residuals which again, indicates that the GDHC correlations did not converge properly. The strains in ε_{ll} and ε_{tt} (Figure C-2b,c) represent similar outcome as gained with the 4th order polynomial only

the strain fields have more fluctuations over the whole surface. In conclusion, the correlations seem to generate unreliable information.

The solution for this problem can be found in the quality of the images which are made with the Bruker NPFlex or it can come due to the GDHC correlations. Therefore, a small optimization step is needed to improve the reliability of the outcome.
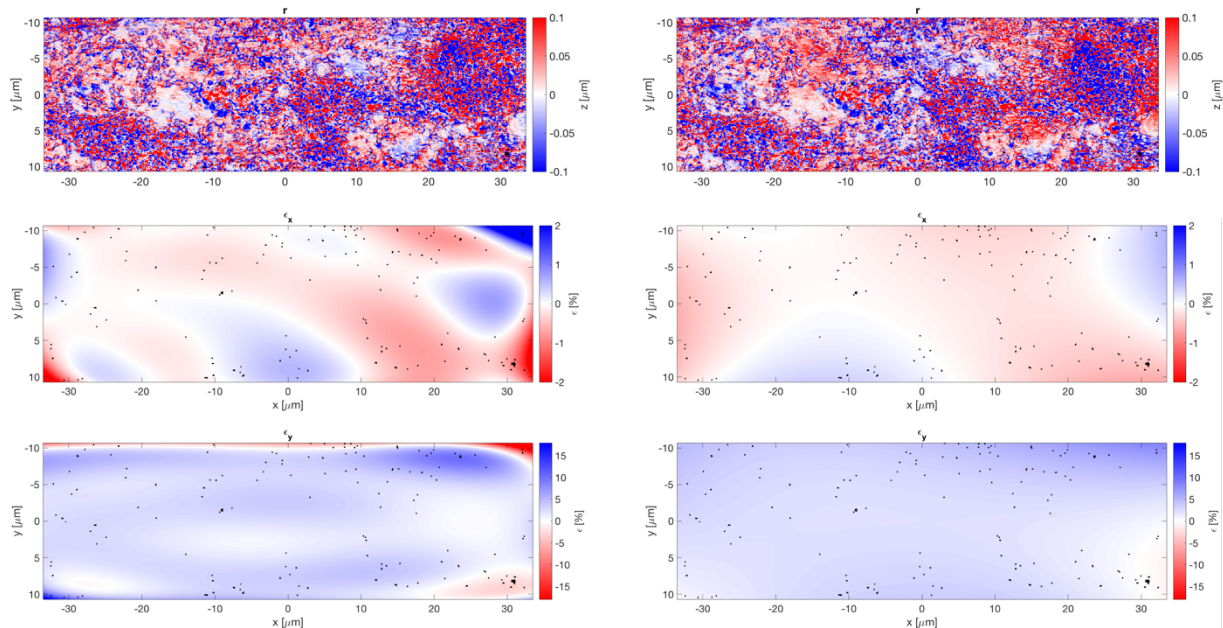

Figure C-2: Outcome of the correlation between the first image and the last images of the experiment, left gained outcome with the 8th order polynomial shape function, right gained outcome with the 4th order polynomial shape function.

Left (8th order polynomial shape function): (a) The residual field, (b) Longitudinal strain and (c) transverse strain.

Right (4th order polynomial shape function): (d) The residual field, (b) longitudinal strain and (c) transverse strain.

Final small optimization step

The final small optimization can be found in the GDHC correlations and in the quality of the topography images. The optimization for the GDHC correlations can be found in the creation of the reconstructed height data in the deformed image g. Besides the reconstructed height data also the dilatation of the masking feature has an influence on the noise during the correlations.

The quality of the topography images is important since the images can contain areas which are sensitive for noise during measurements. These areas can therefore fluctuate between different topography images which will result in high residuals. These sensitive areas can come due to the settings of the Bruker NPFlex or the environment.

GDHC correlation

An importation optimization of the GDHC correlation is the creation of the reconstructed height data. This reconstructed data is created to replace the NaN values in the deformed image g. Previously, the NaN values in the deformed image g are replaced with the mean height of the fiber surface in

the deformed image g. This can lead to large residuals because the reconstructed height data can influence large height fluctuations between the actual fiber surface height and the reconstructed data. This problem is tackled by the use of a linear interpolation step. All the NaN values in the deformed image g will be replaced by interpolation of the surrounded values which creates more valid and realistic reconstructed height data.

Besides the added interpolation step, the dilatation of the mask in the reference image f is changed to 2 rows around a NaN filled pixel. Since the pattern on the fiber surface consist of nano particle with steep edges it is favorable to mask the edges of these nano particles since steep edges can be a source of large residuals.

Magnification

By using the internal 2x lens more detailed topography images can be obtained of the fiber surface. The topology features and the particles on the fiber surface can be better visualized and are therefore better trackable during GDHC correlations. By using the internal 2x lens the field of view reduces from 80 x 60 μm to 40 x 30 μm. However, this makes the measurements also more sensitive to environmental influences like, vibrations, air flow and light. The influences from the air flow in the lab are reduced by closing the surrounded box around the Bruker NPFlex. This creates an area inside the box without any air flow which is favorable for such sensitive measurements. The light is eliminated by covering the whole box by black foil so no environmental light can enter the larger box and can influence the measurements.

Threshold

Previous correlations showed noisy areas with large residuals and areas with small residuals. Figure C-3 shows the residual field of the previous experiment between the first and second topography images which were taken with an automatic light intensity of 23% and a threshold of 2%. Figure C-3 visualizes the noisy areas and the areas with much lower residuals.
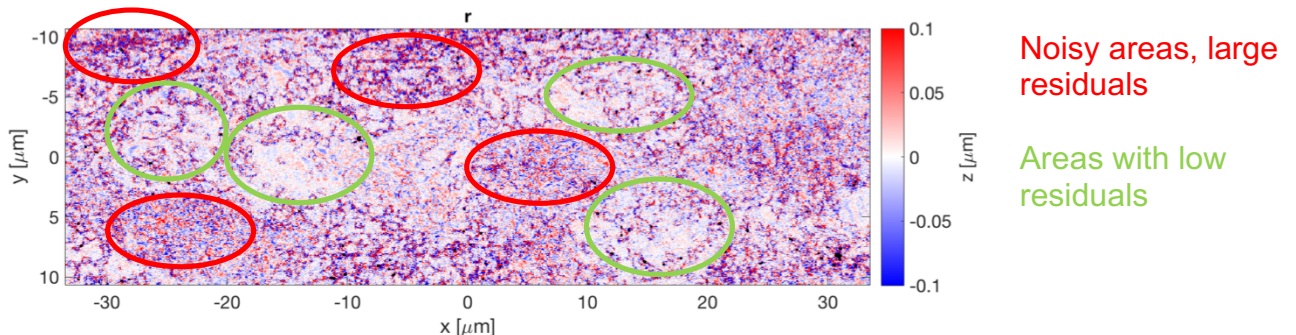

Figure C-3: The residual field of the previous experiment between the first and second topography image.

It is likely that the correlations went incorrect because of the noisy areas even after the first GDHC correlation. These noisy areas are relatively large compared with the areas with low residuals. A known fact is that by higher thresholds less height information is used to create the images.
The hypothesis is that with a higher threshold in combination with the above mentioned improvements the noisy areas will be reduced which results in improved correlations with a lower RMS of the residual field. This hypothesis is verified with a simple test. Different thresholds in combination with the above mentioned optimizations are set during 4 rigid body motions of 0.5 μm in x- and y-direction. The RMS of the residual fields will give an inside in the influence of the final small optimization step. Figure C-4 represents a graph of the RMS of the residual fields after 4 rigid body motions for different thresholds and different polynomial orders (0, 1 or 2). The line with the * marks represents the correlations which were done without the small optimization step namely, without the interpolation of the reconstructed data, a threshold of 2% and without the use of the internal 2x lens. The graph already confirms the hypothesis; i.e. by increasing the threshold the RMS of the residual field will decrease.
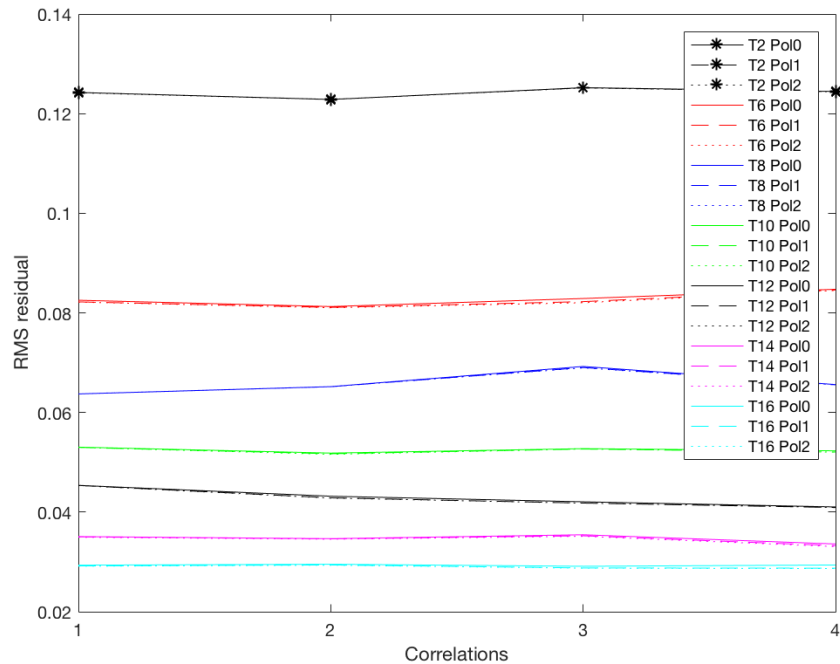

Figure C-4: The RMS of the residual fields for 4 rigid body motions for different settings.

The hypothesis is even more confirmed when looking at the different residual fields. Figure C-5 represents the residual fields of a simple rigid body motion were the threshold of the Bruker NPFlex was set to 6%, 10% and 16%. The high error areas in residual fields decreases and are replaced with NaN values (black) when increasing the threshold. This confirms that the sensitive areas,

which are high error sources during correlations, in reference image f and g are ignored due to the use of higher thresholds. At a certain time, the threshold will be chosen too high which results in ignoring robust areas were lower residuals will occur. This is unfavorable since enough robust height information of the fiber is necessary to calculate the strains over the whole fiber surface. Therefore, the choice of the threshold has an influence on reducing the high error areas but also on reducing the amount of robust height information. A threshold between 10 or 12% is used during further experiments since these thresholds seem to be the best trade-off of ignoring the high error areas and preserving the most robust height information. Besides the threshold also the interpolation scheme for creating reconstructed data and the internal 2x lens are used during further experiments.
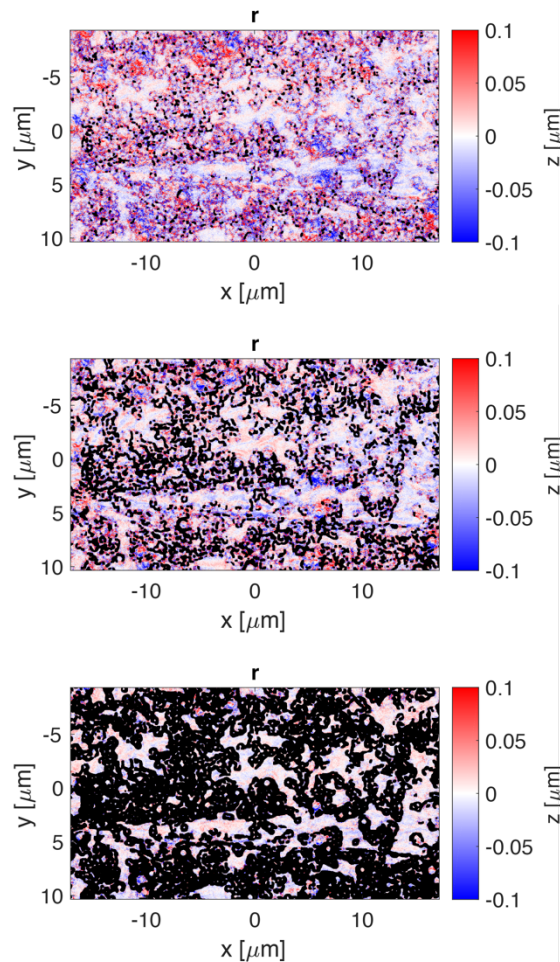

Figure C-5: The residual fields after correlating a simple rigid body motion. The topography images are taken with a threshold of (a) 6%, (b) 10% and (c) 16%.

<u>Order shape function:</u>

As mentioned earlier it is important to use a minimum order of the basis function which is sufficient enough to capture the whole kinematics of the fiber. An experiment is conducted to determine the order of the shape function to check if the 4th order polynomial from Bastawrous [8] is sufficient. In the experiment the sample undergoes a humidity program in time. First the sample is conditioned at 50% RH at 23°C for an hour. After this hour the humidity is increased to 80% RH at 23°C with a rate of 10% RH/hour. After this increase the humidity is fixed at 80% for two hours to let the fiber relax. For the experiment 419 images were made with a threshold of 12% and the order of the polynomial shape functions is determined by looking at the RMS of the residual fields. Figure C-6 represents the RMS of the residual fields for different order of the polynomial shape function. The colors represent the RMS of the residual fields of 10 correlations which were done around a specific relative humidity (50%, 60%, 70% and 80% RH). The RMS of the residual fields around 50%, 60% and 70% relative humidity seem to reach a plateau value at a 1st order polynomial shape function. Higher order shape functions are not resulting in lower RMS of the residual fields but it will only over capture the whole kinematics of the fiber which is unfavorable. The RMS of the residual fields around 80% relative humidity keeps decreasing even with higher order polynomial shape functions. From this we can conclude that a 1st order shape function would be sufficient. Since a fiber has an elliptical shape, membrane shaped deformations can occur as well and these deformations cannot be captured by the 1st order polynomial shape function. With that in mind, the order of the shape function is chosen to be 2nd order to capture also these membrane shaped deformations.
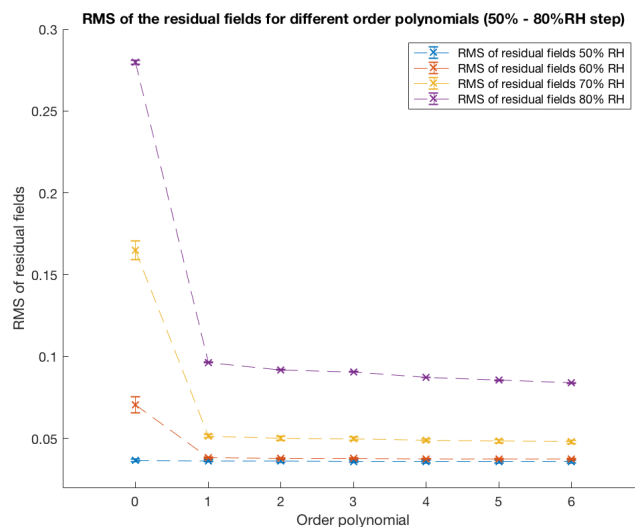

Figure C-6: The RMS of the residual fields for different order of the shape function. The different colors show the RMS of the residual fields around 50% RH, 60% RH, 70% RH and 80% RH.

Conclusion of the optimized GDHC settings

Coarse grain step:
As described earlier, Coarse graining is set to 0, since fibers have a relative flat surface will low gradients.

Convergence criterion:
As described earlier, the convergence criteria is at $\|\delta\lambda\|$<10^{-4}.

Maximum iterations:
The maximum iterations is set to 500.

Basis shape function:
As described earlier, the polynomial basis shape function was chosen to describe the displacement field.

Order shape function:
As described earlier, the order of the polynomial shape function was chosen to be 2nd order.

Masking:
As described earlier, the dilatation of the mask in the reference image f is changed to 2 rows around a NaN filled pixel. Since the pattern on the fiber surface consist of nano particle with steep edges it is favorable to mask the edges of these nano particles since steep edges can be a source of large residuals.

Reconstructed height data:
As described earlier, all the NaN values in the deformed image g will be replaced by interpolation of the surrounded values which creates more valid and realistic reconstructed height data.

Gradient:
As described earlier, gradient of f is chosen since it takes the gradient of the reference image and not from de deformed image. Taking the gradient of the deformed image will introduce noise since the NaN filled pixels are replaced with reconstructed data.